J. Fluid Mech. (2010), *vol.* 642, *pp.* 235–277.
doi:10.1017/S0022112009991819

Evolution of solitary waves in a two-pycnocline system

M. NITSCHE[1]†, P. D. WEIDMAN[2], R. GRIMSHAW[3], M. GHRIST[4] AND B. FORNBERG[5]

[1]Department of Mathematics and Statistics, University of New Mexico, Albuquerque, NM 87131, USA

[2]Department of Mechanical Engineering, University of Colorado, Boulder, CO 80309-0427, USA

[3]Department of Mathematical Sciences, Loughborough University, Loughborough, LE11 3TU, UK

[4]Department of Mathematical Sciences, USAF Academy, CO 80840-6252, USA

[5]Department of Applied Mathematics, University of Colorado, Boulder, CO 80309-0526, USA

(Received 4 March 2009; revised 30 July 2009; accepted 26 August 2009;
first published online 11 December 2009)

Over two decades ago, some numerical studies and laboratory experiments identified the phenomenon of leapfrogging internal solitary waves located on separated pycnoclines. We revisit this problem to explore the behaviour of the near resonance phenomenon. We have developed a numerical code to follow the long-time inviscid evolution of isolated mode-two disturbances on two separated pycnoclines in a three-layer stratified fluid bounded by rigid horizontal top and bottom walls. We study the dependence of the solution on input system parameters, namely the three fluid densities and the two interface thicknesses, for fixed initial conditions describing isolated mode-two disturbances on each pycnocline. For most parameter values, the initial disturbances separate immediately and evolve into solitary waves, each with a distinct speed. However, in a narrow region of parameter space, the waves pair up and oscillate for some time in leapfrog fashion with a nearly equal average speed. The motion is only quasi-periodic, as each wave loses energy into its respective dispersive tail, which causes the spatial oscillation magnitude and period to increase until the waves eventually separate. We record the separation time, oscillation period and magnitude, and the final amplitudes and celerity of the separated waves as a function of the input parameters, and give evidence that no perfect periodic solutions occur. A simple asymptotic model is developed to aid in interpretation of the numerical results.

Key words: internal waves, solitary waves

1. Introduction

A pycnocline is a thin horizontal transition region between fluids of different densities. Pycnoclines occur, for example, in the ocean between regions of different salinity. Disturbances of the pycnoclines, caused perhaps by tidal currents over bottom topography or by moving submarines, can result in large-amplitude internal waves (see Grimshaw 2001 and Helfrich & Melville 2006 for recent reviews), and hence it is of interest to determine how far and how fast these disturbances travel alone or in groups.

† Email address for correspondence: nitsche@math.unm.edu

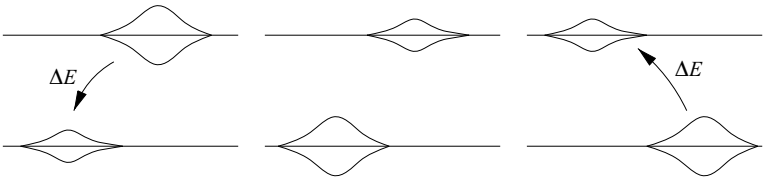

FIGURE 1. Sketch of backward (downstream) energy transfer between waves on separate pycnoclines.

Much is known about disturbances on a single pycnocline. The governing Korteweg–de Vries (KdV) equations were derived by Kubota, Ko & Dobbs (1978) and it is well known that most initial conditions will evolve into disturbances that travel downstream as a series of ordered solitary waves followed by a dispersive tail (see e.g. Segur 1973). Moreover, overtaking solitary wave interactions are characterized by a forward or *upstream* transfer of energy from an initially larger fast-moving trailing wave to a smaller slower lead wave.

In a seminal study, Liu, Kubota & Ko (1980) reported the resonant energy transfer that can occur between weakly nonlinear long internal waves travelling on separate pycnoclines with nearly equal linear phase speeds. Denoting a typical wavelength by λ and pycnocline separation by H, they derived a pair of governing KdV equations, coupled through the dispersion terms, valid for $H/\lambda = O(1)$. Numerical integration for a system of mode-two waves showed their evolution into a nearly periodic leapfrog motion. They were the first to reveal the backward or *downstream* energy transfer from the larger amplitude lead wave on one pycnocline to the smaller amplitude trailing wave on the neighbouring pycnocline which results in an exchange in wave amplitude; the now larger trailing wave then hops past the smaller lead wave as illustrated in figure 1. Since integrations were carried out to only three hops, the long-time behaviour of the system was not determined.

In a following study, Liu, Pereira & Ko (1982) modelled the weak coupling between internal waves on separate pycnoclines using Joseph (1977) mode-two solitary wave solutions to obtain an approximate analytic formula for the frequency of leapfrog oscillation. The weak coupling assumption is satisfied when $H/\lambda \gg O(1)$. They found that the oscillation frequency ω is significantly smaller than the frequency ω_{BO} (Benjamin 1967; Ono 1975) for oscillations of mode-two Benjamin–Ono (BO) solitary waves.

Leapfrog oscillations of mode-two solitary waves were first realized in laboratory experiments performed by Weidman & Johnson (1982) (referred to as WJ). The experiments were performed in a 10 m channel in which the initial two-pycnocline stratification was constructed using saline water. Under the gravitational collapse of two uniformly mixed regions at one end of the tank, mode-two waves formed, travelled down the tank and reflected at the endwall resulting in as many as five visible hops. Measurements of solitary wave amplitudes and positions, taken after an initial adjustment period in which dispersive waves were shed, exhibited the leapfrog dynamics. Here in figure 2 we reproduce (from figure 6*a* of Weidman & Johnson 1982) measured wave evolutions in which the downward (upward) triangles correspond to lower (upper) wave amplitudes a_i in centimetres. The mean system amplitude $\overline{a}$ shown by the dotted line exhibits strong attenuation. This amplitude decay was attributed to the viscous dissipation of the individual waves; see, for example, the comparison of measured attenuation of free surface solitary waves with the theory of Keulegan (1948) in Weidman & Maxworthy (1978). From the WJ experiments it is clear that the long-time evolution of the system cannot be determined. Weidman and Johnson

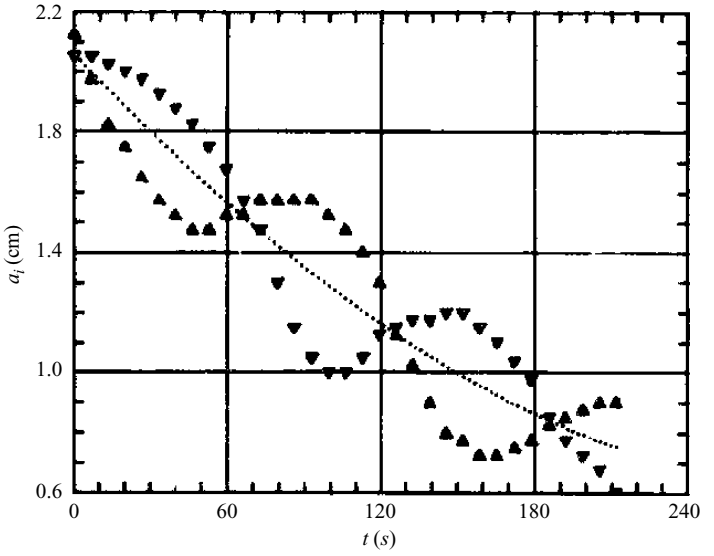

FIGURE 2. WJ measurements of wave amplitudes versus time. Upward and downward triangles denote the amplitude of the upper and lower pycnocline, respectively.

conjectured that, in the absence of viscous dissipation, the long-time evolution would be, as suggested in Liu *et al.* (1980), simple periodic leapfrog motion.

In a couple of instances in the WJ experiments, two solitary waves ordered in amplitude evolved along each pcynocline from the collapsed mixed regions. In one such realization, a lead and trailing wave on one pycnocline interacted with the lead wave on the neighbouring pycnocline, the remaining trailing wave having been left behind. This resulted in a three-wave interaction which combines both *upstream* and *downstream* energy transfer. Again, dissipation precluded evaluation of the long-time behaviour of this curious interaction. Weidman & Johnson (1982) conjectured that the ideal (inviscid) three-wave interaction is not one of simple resonance since the time scale for forward energy transfer between waves travelling along the a given pycnocline is faster than the rearward energy transfer between waves on neighbouring pycnoclines. As a result it was postulated that the motion is either a Fermi–Pasta–Ulam recurrence phenomenon (see Fermi, Pasta & Ulam 1955) or chaotic.

Since the 1982 appearance of the WJ experimental results, one of us (PW) has been interested in numerically finding the asymptotic behaviour of the two-wave and three-wave mode-two interactions on separate pycnoclines. At that time, scientists at the National Center for Atmospheric Research (NCAR, Boulder) and Scripts Institute of Oceanography (La Jolla) advised that the accuracy of very long-time integrations could not be ensured. The difficulty arises from the high resolution needed to obtain accurate and stable results, since the high wavenumbers are highly unstable, and the low wavenumbers need to be computed with high accuracy. Recently, however, Fornberg & Driscoll (1999) presented a spectral method in which high and low wavenumbers are resolved using different numerical schemes. In our study we apply such a spectral method to the two-pycnocline problem and resolve the two-wave system to very large times.

Following publication of the WJ experiments, there have appeared at least three studies of leapfrogging KdV solitary waves. First and foremost is the work of Gear & Grimshaw (1984) who derived a set of amplitude equations for the interaction of weakly nonlinear internal gravity waves on pycnoclines not widely separated,

$H/\lambda \ll 1$. The equations describing this system are both nonlinearly and dispersively coupled. Integrations for realistic Brunt–Väisälä frequencies reveal that the upper and lower disturbances evolve, after an initial adjustment, into a completely phase-locked non-oscillatory solitary wave system. When the coefficients of the nonlinear terms are set to zero, on the other hand, the system evolves into a quasi-periodic state with upper and lower amplitudes continually exchanging energy, closely resembling the leapfrog results found in Liu *et al.* (1980) and Liu *et al.* (1982). However, Gear and Grimshaw carefully note that complete periodicity is not attained, as some trailing radiation is continually being formed. Should this also occur for $H/\lambda = O(1)$, an asymptotic periodic leapfrog behaviour of the LKK system would not be possible.

Malomed (1987) also studied the LKK equations coupled only through dispersion. Using the adiabatic approximation, he finds *inter alia* (i) an estimate of the frequency of small oscillations in the vicinity of equilibrium and (ii) the power radiated in the form of small-amplitude quasilinear waves from leapfrogging solitons. Not surprisingly, he finds that the frequency of radiation coincides with the frequency of soliton oscillation. No mention is made of the possible long-time behaviour of the system.

Wright & Scheel (2007) analyse the linear stability of a coupled pair of evolution equations which include those of Gear & Grimshaw (1984) as a special case. They find that the system is linearly unstable and conclude that the slowly growing oscillatory instability is the origin of the leapfrogging behaviour described in previous literature. As a numerical example, they integrate a pair of equations coupled only nonlinearly through parameter ϵ. For $\epsilon < 0$ leapfrog oscillations are found with waves radiating behind the travelling wave system. When the integration is carried out to long times the amplitudes decrease, the spatial oscillations grow and eventually the interaction ceases at which point the waves separate as individual solitary waves. Thus leapfrogging is a transient behaviour for the KdV equations coupled only through nonlinearity.

In view of these studies, we might anticipate that the leapfrog behaviour observed in the LKK equations coupled only through dispersion is also just a transient phenomenon. Indeed, within the solution space for which the waves oscillate, our extensive numerical results show that eventually the waves separate as discrete solitary waves, no longer shedding dispersive waves in their wake. For certain values of the density parameters, however, the oscillations persist for a very long time. We record the separation time, oscillation magnitude and period and final speed as a function of the environmental parameters.

The paper is organized as follows. Section 2 introduces the physical problem to be simulated in this paper and all relevant dimensionless parameters. Section 3 describes the modelling equations and the initial conditions incorporated. Section 4 outlines the numerical method and our numerical results are presented in § 5. A simple asymptotic model for the leapfrog oscillation frequency is given in § 6 and our findings are summarized in § 7. An alternative derivation of the governing equations is presented in the Appendix.

2. Problem description

The system of interest here is best described by the experiment presented in Weidman & Johnson (1982). In the experimental procedure a tank 10 m long, 20 cm wide and 30 cm deep is filled, first with water of high salinity, followed with water of medium salinity, and then with water of low salinity, forming a stable three-layer stratification with $\rho_3 > \rho_2 > \rho_1 \geqslant 1$ and heights H_3, H_2, H_1, as indicated in figure 3. The upper surface in the experiments was free. Typical experimental values are $\rho_1 = 1.02$,

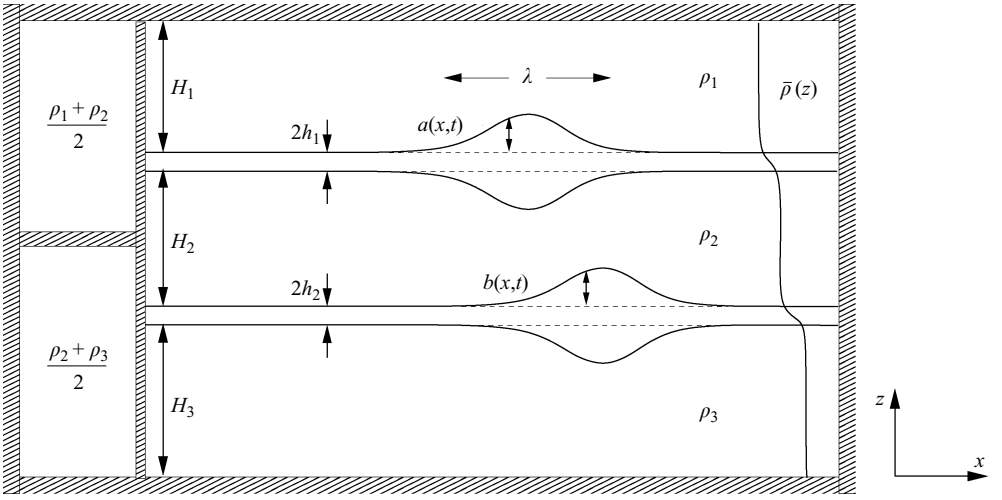

FIGURE 3. Sketch of experimental set-up and relevant parameters.

$\rho_2 = 1.05$ and $\rho_3 = 1.08$ g cm^{-3} with separation distances $H_1 = 8.0$, $H_2 = 15.0$ and $H_3 = 8.0$ cm. The three layers of constant density are separated by two thin transition layers across which the density varies in hyperbolic tangent fashion. The thicknesses $2h_1$ and $2h_2$ of the upper and lower pycnoclines, respectively, grow slowly after formation due to diffusion. Since the lower layer is formed first, by the same floating raft technique, necessarily $h_1 \leqslant h_2$. Typical experimental values are $h_1 = 1.8$ cm and $h_2 = 2.0$ cm. The composite density profile across the tank is denoted by $\overline{\rho}(z)$ in figure 3, where z is the height above the bottom of the tank.

Simultaneous generation of mode-two waves on the separate pycnoclines was formed as follows. At one end of the tank a permanent horizontal splitter plate 40 cm long is located at mid-depth. A removable vertical barrier is located at the end of the splitter plate. After stratifying the tank, the vertical barrier is gently inserted and the fluid behind is uniformly mixed in the upper and lower chambers. As a result of the near symmetry of the system, intermediate densities $(\rho_2 + \rho_3)/2$ and $(\rho_1 + \rho_2)/2$ are formed as illustrated in the sketch in figure 3. Upon removing the vertical barrier, the fluid in the upper and lower compartments collapse into their respective pycnoclines forming bulges of locally increased pycnocline thickness. These bulge waves deplete the mass they carry and evolve into separate mode-two solitary waves, one above the other, with similar dispersive tails. Owing to small differences in pcynocline thickness and other initial conditions, one wave (generally the lower) moves slowly ahead of the other and initiates the leapfrog motion, both lead waves having left their dispersive tails behind. The disturbance amplitudes $a(x, t)$, $b(x, t)$ have characteristic wavelengths λ, as indicated in figure 3, where x is the direction along the tank and t is time.

We numerically simulate the evolution of mode-two disturbances on separate pycnoclines not obstructed by endwalls, in the absence of viscous diffusion. We solve the model equations of Liu *et al.* (1980) for the case $\lambda = O(H_2)$, described next, using an accurate spectral method and compute the solutions for a range of input parameters h_2, ρ_2 and ρ_3, using fixed values of H_1, H_2, H_3, h_1 and ρ_1 comparable to the experimental ones. The upper surface is bounded by a solid wall while in the experiment the upper surface was free. But as a direct comparison is not possible

with experiment owing the ideal fluid assumption in the LKK model, this is of no consequence for the present study.

3. Governing equations

3.1. *Evolution equations*

The asymptotic evolution equations governing the motion of disturbances on two resonantly coupled pycnoclines were first derived by Liu *et al.* (1980). An alternative derivation is presented in the Appendix. Unless otherwise noted, all quantities herein are non-dimensionalized using h_1 as the length scale and $\sqrt{h_1/g}$ as the time scale (g is gravity); the density field is scaled by a constant reference density ρ_0. The equations are expressed in terms of the variables, $A(\xi, T)$, $B(\xi, T)$ where to leading order the streamfunctions in the upper (U) and lower (L) pycnoclines are respectively given by $A\phi_1(z)$, $B\phi_2(z)$ where $\phi_{1,2}(z)$ are the linear long-wave modal functions in each pycnocline, and are defined by (3.4*a*) below. The basic set-up is described in figure 3. Here $\xi = x - c_0 t$ is the spatial variable in the frame of reference moving with the resonant linear long-wave speed c_0, and T is the time variable describing the slow evolution in this frame. The equations are derived for weakly nonlinear waves, and for long waves with characteristic wavelength $\lambda \gg h_{1,2}$, but $\lambda \sim H_{1,2,3}$ is comparable with the layer depths.

Thus the basic equations are (see A27–A33)

$$A_T - \Delta A_\xi + \alpha_1 A A_\xi + \beta_1 \frac{\partial^2}{\partial \xi^2}\left[\frac{\rho_1}{\rho_2}\mathscr{H}_1(A) + m_1^2\,\mathscr{H}_2(A) - m_1 m_2 \mathscr{H}(B)\right] = 0, \quad (3.1a)$$

$$B_T + \Delta B_\xi + \alpha_2 B B_\xi + \beta_2 \frac{\partial^2}{\partial \xi^2}\left[\frac{\rho_3}{\rho_2}\mathscr{H}_3(B) + m_2^2\,\mathscr{H}_2(B) - m_1 m_2 \mathscr{H}(A)\right] = 0, \quad (3.1b)$$

where the operators are defined by

$$\mathscr{H}_j(A) = -\frac{1}{2H_j}\int_{-\infty}^{\infty} A(\tilde{\xi}, T)\coth\frac{\pi(\xi - \tilde{\xi})}{2H_j}\,\mathrm{d}\tilde{\xi}, \quad (j = 1, 2, 3) \quad (3.2a)$$

$$\mathscr{H}(A) = -\frac{1}{2H_2}\int_{-\infty}^{\infty} A(\tilde{\xi}, T)\tanh\frac{\pi(\xi - \tilde{\xi})}{2H_2}\,\mathrm{d}\tilde{\xi}, \quad (3.2b)$$

while the coefficients are given by

$$\alpha_{1,2} = \frac{3}{2}\frac{\displaystyle\int_{U,L}\overline{\rho}(\phi'_{1,2})^3\,\mathrm{d}z}{\displaystyle\int_{U,L}\overline{\rho}(\phi'_{1,2})^2\,\mathrm{d}z}, \quad \beta_{1,2} = \frac{1}{2}\frac{c_{1,2}\rho_2}{\displaystyle\int_{U,L}\overline{\rho}(\phi'_{1,2})^2\,\mathrm{d}z}, \quad (3.3)$$

and

$$(\overline{\rho}\phi'_{1,2})' - \frac{\overline{\rho}'}{c^2}\phi_{1,2} = 0, \quad \phi'_{1,2}(z^{\pm}_{1,2}) = 0 \quad (3.4a)$$

$$\text{with} \quad \phi_1(z_1^+) = 1, \quad \phi_1(z_1^-) = m_1, \quad \phi_2(z_2^-) = -1, \quad \phi_2(z_2^+) = m_2, \quad (3.4b)$$

where $z^{\pm}_{1,2}$ are defined by (A2) in the Appendix and the prime denotes differentiation with respect to z. The modal equations (3.4*a*) are to be solved under the constraint that the linear long-wave speeds are such that $c = c_{1,2} = c_0 \pm \Delta$, which serves to define both c_0 and Δ.

In general, there is an infinite set of modes ϕ_1 and another infinite set of modes ϕ_2, which can be resonant, that is, $c_1 \approx c_2$. Here we are concerned only with the

lowest non-trivial mode, which is defined by that which has just one internal zero for $\phi_{1,2}$ in U, L respectively. For these modes, $\phi'_{1,2} \geqslant 0$ and so both $\alpha_1, \alpha_2 > 0$. Then it follows that we expect solitary-like waves will be elevation waves on each interface, that is $A, B > 0$ for such solutions. Further, following Liu *et al.* (1980), we will assume that $m_1 \approx -1, m_2 \approx 1$ (within 2 % of the actual values), which is valid in the Boussinesq approximation that we will use here, that is, the density jumps are small, $(\rho_2 - \rho_1)/\rho_2 \ll 1$, $(\rho_3 - \rho_2)/\rho_2 \ll 1$, and are significant only when combined with gravity, so that only the reduced gravity terms $g(\rho_1 - \rho_2)/\rho_2$, $g(\rho_2 - \rho_3)/\rho_2$ are retained. The outcome is that the simplified equations we shall solve are

$$A_T - \Delta A_\xi + \alpha_1 A A_\xi + \beta_1 \frac{\partial^2}{\partial \xi^2} [\mathscr{H}_1(A) + \mathscr{H}_2(A) + \mathscr{H}(B)] = 0, \tag{3.5a}$$

$$B_T + \Delta B_\xi + \alpha_2 B B_\xi + \beta_2 \frac{\partial^2}{\partial \xi^2} [\mathscr{H}_3(B) + \mathscr{H}_2(B) + \mathscr{H}(A)] = 0, \tag{3.5b}$$

while the coefficients are again determined as above.

The lowest non-trivial $\phi_{1,2}$ modes are called 'mode-two' waves, since on each pycnocline, the streamfunction amplitudes at the top and bottom boundaries are $\pm A, \pm B$ respectively. It is pertinent to note that a 'mode-one' solution of (3.4*a*) is technically allowed, namely $\phi_{1,2} = 1$, but the speed is infinite, since the corresponding eigenvalue is $1/c_{1,2}^2 = 0$, and so such modes are excluded here. As noted by one reviewer, in a real flow mode-two waves interact with mode-one waves which causes them to decay by radiation damping. This was first shown by Akylas & Grimshaw (1992). However, this result is not directly relevant to our present theoretical and numerical results, since our asymptotic development eliminates mode-one waves. As is now well known, the mode-one waves with a resonant finite wavenumber have exponentially small amplitudes with respect to the amplitudes of the mode-two waves we study, and hence cannot be found with our asymptotic development. The governing equations we use are (3.1) (simplified a bit to (3.5)), which govern the evolution of mode-two waves. The statement that the asymptotically reduced modal system (3.4) has a mode-one wave with infinite speed reflects the fact that mode-one wave solutions of the full eigenvalue problem (A 3) will have, in the long-wave limit $k \to 0$, speeds which scale with $[g' H_1 H_2/(H_1 + H_2)]^{1/2}$, $[g' H_3 H_2/(H_3 + H_2)]^{1/2}$ in the Boussinesq approximation, where g' is reduced gravity. These become infinite with our asymptotic scaling.

To interpret our numerical results it is also pertinent to note that the relationship between $A(\xi, T)$, $B(\xi, T)$ and the pycnocline shapes follows from the fact that, to leading order, the vertical particle displacements ζ are given by

$$c_o \zeta \approx \psi. \tag{3.6}$$

Our choice of a mode-two modal function as above implies that $c_0 \zeta(z = z_1^{\pm}) \approx \pm A(\xi, T)$, $c_0 \zeta(z = z_2^{\pm}) \approx \pm B(\xi, T)$, and therefore corresponds to symmetrically disturbed pycnoclines, with amplitudes $\pm a(\xi, T), \pm b(\xi, T)$ at the bottom boundaries of the upper and lower pycnoclines U, L respectively, given by

$$a(\xi, T) \approx \frac{A(\xi, T)}{c_0}, \quad b(\xi, T) \approx \frac{B(\xi, T)}{c_0}. \tag{3.7}$$

3.2. *Initial conditions*

We are interested in investigating oscillatory solutions to (3.5) and their long-time behaviour. To that effect we use initial data previously shown to lead to oscillating

solutions. Following Liu *et al.* (1982), we use steady-state mode-two Joseph (1977) solitary wave solutions on each pycnocline given by

$$A(\xi,0)=\frac{A_0(1+\cos\delta_1)}{\cos\delta_1+\cosh\left(\frac{\delta_1}{H_1}\xi\right)},\quad B(\xi,0)=\frac{B_0(1+\cos\delta_2)}{\cos\delta_2+\cosh\left(\frac{\delta_2}{H_3}\xi\right)},\tag{3.8a}$$

where $\delta_{1,2}$ are solutions of

$$\delta_1\tan\left(\frac{\delta_1}{2}\right)=\frac{C_1A_0H_1}{c_1h_1^2},\quad \delta_2\tan\left(\frac{\delta_2}{2}\right)=\frac{C_2B_0H_3}{c_2h_2^2},\tag{3.8b}$$

where $C_{1,2}$ are dimensionless constants, and A_0, B_0 are the maximum amplitudes of the initial profiles $A(x,0)$, $B(x,0)$. Note that when $H_1=H_2=H_3$, $C_{1,2}/(c_{1,2}h_{1,2}^2)=\alpha_{1,2}/(4\beta_{1,2})$. These initial conditions are then determined by specifying the input parameters A_0, B_0, H_1, H_2, H_3, h_1, h_2 and the density profile in each pycnocline. In all our numerical results we set $H_1=H_2=H_3$, and we fixed $C_{1,2}/c_{1,2}=4\sqrt{gh_1}/5$, these being representative values for the hyperbolic tangent density profiles we used. In some cases this implies that our initial conditions may not be very close to the actual Joseph solitary waves, but nonetheless there is then a rapid transient adjustment to a state close to a solitary wave solution.

3.3. *Waveforms*

The waves that evolve from the above initial conditions ultimately separate into two distinct solitary waves. According to the derivation of the evolution equations in the Appendix, these primary waves of elevation are properly designated $A(\xi,T)$ and $B(\xi,T)$ and the evolution of these waves will be displayed using these variables. The waveforms in our mathematical model uniquely correspond to mode-two displacements of the pycnoclines. In the experiments of Weidman & Johnson (1982), the pycnocline deflections were visualized by dropping red tracer droplets of a density-controlled kerosene–Freon mixture to predetermined levels above and below the middle of the hyperbolic tangent density profiles near the extrema of the spatial eigenfunction for each wave (cf. figure 4 of Weidman & Johnson 1982 which shows a complete period of leapfrog motion visualized by the kerosene–Freon droplets).

To orient the reader to the time evolution figures of travelling waves presented in the coming sections, we show in figure 4, at arbitrary fixed time T, the correspondence between the upper and lower pycnocline deflections Z_U and Z_L and the amplitudes $A(\xi,T)$ and $B(\xi,T)$ given by (3.7). Figure 4 shows a case when the leapfrog motion has ceased and the waves are separating in time due to their inherent speed difference. These separated waves are steady solitary waves, that is, they propagate, very accurately, without change of form and at constant speed. In figure 4(*a*) the pyclocline deflections Z_U and Z_L are plotted without magnification and in figure 4(*b*) they are seen with a 25-fold magnification. In figure 4(*c*) the pycnocline disturbances characterized by $A(\xi,T)$ (solid line) on the upper pycnocline and $B(\xi,T)$ (dashed line) on the lower pycnocline are displayed.

It should be carefully noted in figure 4(*b*) that a mode-two wave of depression exists on the lower pcynocline immediately beneath the mode-two wave of elevation Z_U on the upper pycnocline; similarly, for the mode-two wave of elevation Z_L on the lower pycnocline, one sees a mode-two wave of depression immediately above on the upper pycnocline. These depression waves are phase-locked signatures of the primary waves travelling on the neighbouring pycnocline, and *together* each constitutes a mode-two solitary wave of the system (3.5). This total wave structure must be kept in mind

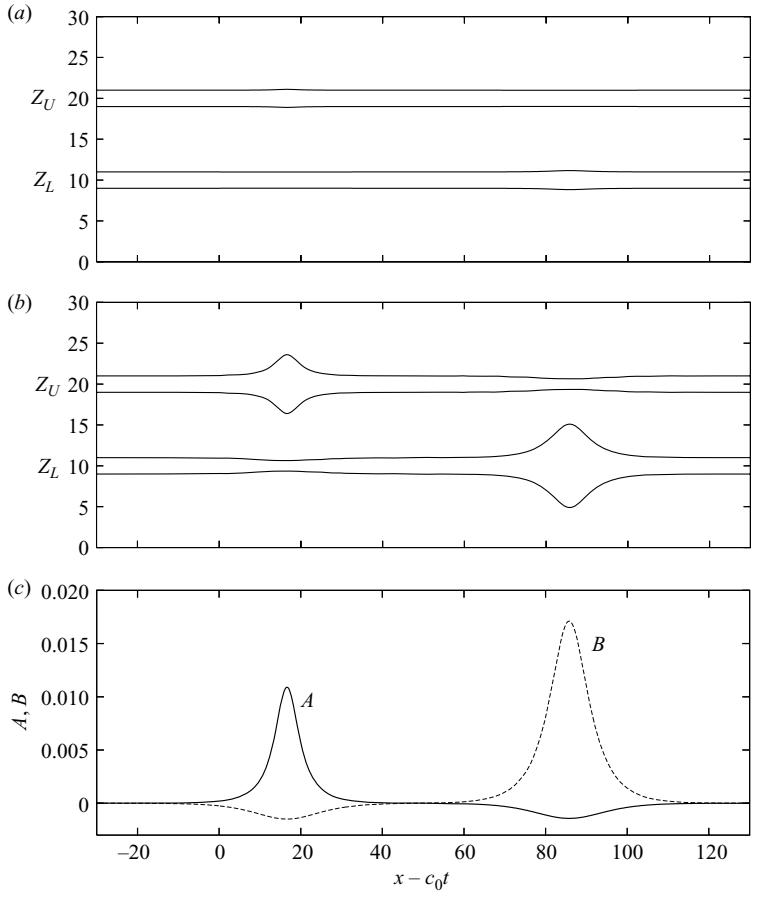

FIGURE 4. Relation between physical waveforms and functions $A(\xi, T)$, $B(\xi, T)$, where $\xi = x - c_0t$. (*a*) Sample shape of a perturbed pycnocline. The curves are given by $z(\xi, T) = H_2 + H_3 \pm (h_1 + \tilde{a}(\xi, T))$ for the top pycnocline, and $z(\xi, T) = H_3 \pm (h_2 + \tilde{b}(\xi, T))$ for the bottom one. (*b*) Amplified pycnocline $z(\xi, T) = H_2 + H_3 \pm (h_1 + 25\tilde{a}(\xi, T))$, $z(\xi, T) = H_3 \pm (h_2 + 25\tilde{b}(\xi, T))$. (*c*) Corresponding values of $A(\xi, T)$ (solid), and $B(\xi, T)$ (dashed), where $A(\xi, T) = \tilde{a}(\xi, T)/c_0$, $B(\xi, T) = \tilde{b}(\xi, T)/c_0$. The actual pycnoclines satisfy $a(\xi, T) \approx \tilde{a}(\xi, T)$, $b(\xi, T) \approx \tilde{b}(\xi, T)$.

when viewing the forthcoming results presented in the succinct figure 4(*c*) format. Also, when the coupling between the two pycnoclines is weak, our initial condition (3.8) can be regarded as a perturbation of this system of two solitary waves, and our numerical results can be interpreted as indicating the stability or otherwise of this system.

4. Numerical method

4.1. *The pseudo-spectral method of Fornberg and Driscoll*

Fornberg & Driscoll (1999) present a spectral algorithm for equations of the general form

$$u_t = \mathcal{N}(u) + \mathcal{L}(u), \tag{4.1}$$

where $u = u(\xi, t)$ is periodic in ξ, $\mathscr{L}$ is linear and consists of the highest order dispersive terms in the equation; $\mathscr{N}$ contains all other possibly nonlinear terms. As an example, consider $\mathscr{L}(u) = d(t)(\partial^{m_o} u/\partial \xi^{m_o})$. With this $\mathscr{L}$, the equation in Fourier space is

$$\frac{\partial \widehat{u}_k}{\partial t} = \widehat{\mathscr{N}}(\widehat{u}_k) + (\mathrm{i}^{m_o} d) k^{m_o} \widehat{u}_k, \tag{4.2}$$

where $u(\xi, t) = \sum_k \widehat{u}_k(t) \mathrm{e}^{\mathrm{i}k\xi}$. Their goal is to find an accurate and stable method to solve (4.2). Stability is determined from the linearized equation

$$\frac{\partial \widehat{u}_k}{\partial t} = \mathrm{i}\gamma \widehat{u}_k + (i^{m_o} d) k^{m_o} \widehat{u}_k, \tag{4.3}$$

where it is assumed that γ is real and of lower order than m_o in k. Standard explicit time stepping schemes applied to (4.2), such as Runge–Kutta or Adams–Bashforth (AB) methods, have a finite region of stability $|d\, k^{m_o}| \Delta t \leqslant B_M$, where B_M depends on the method M. Thus, the maximal size of permissible time steps is limited by the highest wavenumbers k_{max} to be resolved.

The restriction becomes more severe as m_o and k_{max} increase. Implicit schemes, such as Adams–Moulton (AM) methods, do not have this restriction but are numerically costly since they require inverting a nonlinear system at each time step.

Instead, Fornberg & Driscoll (1999) consider mixed methods to solve (4.2). The basic idea is that (i) the lower order nonlinear portion can be solved with an explicit method, (ii) the linear portion can be solved using different methods for different wavenumbers. In particular, the low modes $|k| < k_1$ can be computed using a highly accurate explicit scheme M. The argument is that the low modes need to be computed accurately, and the required time steps are accuracy limited and not stability limited. Thus, for a given time step Δt required for accuracy, k_1 is chosen so that $|d| k_1^{m_o} \Delta t \leqslant B_M$, ensuring stability. The remaining high modes are computed using a combination of an explicit scheme for the nonlinear part and an implicit scheme for the linear part.

Generally, however, these mixed methods do not preserve the inherent good stability properties of purely implicit schemes. The contribution of Fornberg & Driscoll (1999) is to judiciously construct a combination of a classical fourth-order AB method (AB4) for the linear portion with a modified second-order AM method (AM2*) for the nonlinear portion, for which the resulting stability region is unbounded along the imaginary axis. Since γ and d are assumed to be real, this combination is stable for all time steps. It is used for the highest modes. Fornberg and Driscoll note that the highest modes need not be computed as accurately as the lower ones in order to obtain a prescribed accuracy in real space. For intermediate modes with $|k| \geqslant k_1$ that need to be computed accurately, they propose a higher order implicit scheme for the linear part which, however, lacks the good stability properties of the AB4/AM2* combination.

The particular method proposed by Fornberg and Driscoll (1999) consists of

$$\text{AB4/AB4 for } |k| < k_1, \quad k_1 = \left(\frac{0.40}{|d| \Delta t} \right)^{1/m_0}, \tag{4.4a}$$

$$\text{AB4/AM6 for } k_1 \leqslant |k| < k_2, \quad k_2 = \left(\frac{1.31}{|d| \Delta t} \right)^{1/m_0}, \tag{4.4b}$$

$$\text{AB4/AM2}^* \text{ for } |k| \geqslant k_2. \tag{4.4c}$$

Here a pair of methods, such as AB4/AM6, refers to the methods applied to the nonlinear/linear parts respectively. The values of k_1 and k_2 are determined using the stability regions of AB4 and AB4/AM6, respectively. To account for non-zero γ we used the values listed above which are slightly lower than the ones listed in Fornberg & Driscoll (1999).

In this paper we apply the FD method to solve the system of equations (3.5). The equations are first written in Fourier space and linearized to find the values of d and m_o corresponding to the system. Assuming that $A(\xi, T)$ and $B(\xi, T)$ are periodic in $[-L, L]$, and that space is discretized by $\xi_j = -L + \frac{2Lj}{N}$, $j = 1, \ldots N$, we approximate (3.5) in Fourier space by

$$\frac{\mathrm{d}}{\mathrm{d}T}\widehat{A}_k = \widehat{\mathscr{N}}^1_k(A) + \widehat{\mathscr{L}}^1_k(A, B), \tag{4.5a}$$

$$\frac{\mathrm{d}}{\mathrm{d}T}\widehat{B}_k = \widehat{\mathscr{N}}^2_k(B) + \widehat{\mathscr{L}}^2_k(A, B) \tag{4.5b}$$

for $k = 1, \ldots, N$, where $\widehat{f} = 1/4\pi L \sum_{j=-N/2}^{N/2-1} f(\xi_j)\mathrm{e}^{-\mathrm{i}k\xi_j/(2L)}$ denotes the discrete Fourier transform of generic variable f, and

$$\widehat{\mathscr{N}}^1_k(A) = -\frac{\mathrm{i}k\alpha_1}{2}\widehat{A^2}_k - \mathrm{i}k\Delta c\widehat{A}_k, \qquad \widehat{\mathscr{L}}^1_k(A, B) = \mathrm{i}\beta_1 k^2(d_{11}\widehat{A} + d_{12}\widehat{B}_k), \tag{4.6a}$$

$$\widehat{\mathscr{N}}^2_k(B) = -\frac{\mathrm{i}k\alpha_2}{2}\widehat{B^2}_k + \mathrm{i}k\Delta c\widehat{B}_k, \qquad \widehat{\mathscr{L}}^2_k(A, B) = \mathrm{i}\beta_2 k^2(d_{12}\widehat{A} + d_{22}\widehat{B}_k), \tag{4.6b}$$

where $d_{11} = \coth(H_1 k) + \coth(H_2 k)$, $d_{12} = \mathrm{csch}(H_2 k)$, $d_{22} = \coth(H_2 k) + \coth(H_3 k)$. Thus these equations follow the framework considered by Fornberg & Driscoll (1999) with $m_o = 2$. Note that for the sake of algebraic simplicity, the analysis in Fornberg and Driscoll assumed that the linearized $\widehat{N}$ was purely imaginary, which is not the case here. However, as the present calculations show, the algorithm is sufficiently robust that minor deviations from this assumption do not have any adverse effects. For clarity, we also note that in our case (4.6), $\mathscr{L}$ consists of all the dispersive terms.

For each wavenumber k, (4.5) is a system of two coupled equations to which we apply the method (4.4). The method applied to such a system is stable if d is replaced by an upper bound for the largest eigenvalue of the matrix

$$\begin{pmatrix} \beta_1 d_{11} & \beta_1 d_{12} \\ \beta_2 d_{12} & \beta_2 d_{22} \end{pmatrix},$$

for example,

$$d = \max(\beta_1, \beta_2)\left[\coth(H_1|k|) + \coth(H_2|k|) + \coth(H_3|k|) + \mathrm{csch}(H_2|k|)\right] \geqslant 0. \tag{4.7}$$

We now state the specific steps taken to implement the method described above to solve (3.5). The initial data required for the multistep AM and AB methods are obtained using the fourth-order Runge–Kutta method (RK4) with a time step sufficiently small to maintain stability.

Step 0: Initialization

(*a*) Set number of points N, interval half-length L, final time T_{max}, time step ΔT.

(*b*) Set physical parameters $\rho_{1,2,3}$, $h_{1,2}$, $H_{1,2,3}$ and corresponding values of $c_{1,2}$, $\alpha_{1,2}$, $\beta_{1,2}$, Δc determined by solving (3.3,3.4) as described below in § 4.3.

(*c*) Set $\xi_j = -L + j\Delta\xi$, $j = 1, \ldots N$, $\Delta\xi = 2L/N$ and $M = T_{max}/\Delta T$.

(*d*) Set $A^0_j = A(\xi_j, 0)$, $\quad B^0_j = B(\xi_j, 0)$ according to (3.8).

(*e*) Set k_1, k_2 according to (4.4), (4.7), with $m_o = 2$.

(*f*) Apply RK4 for 40 steps using time step $\Delta T/10$, thus solving the system up to time $4\Delta T$. This step yields the 4 initial approximations $A^m(\xi_j)$ of $A(\xi_j, T_m)$, $m = 1, 2, 3, 4$, $j = 1, \ldots, N$, where $T_m = m\Delta T$, that are needed for the multistep methods used next.

For $m = 4, \ldots M$ perform steps 1–4 to advance in time:

Step 1: Apply AB4 to compute changes in the nonlinear terms, for all k.

(*a*) Compute $\widehat{\mathscr{N}}^{1,m} = \widehat{\mathscr{N}}^1(A^m)$, $\widehat{\mathscr{N}}^{2,m} = \widehat{\mathscr{N}}^2(B^m)$ using (4.6).

(*b*) Set

$$d\widehat{\mathscr{N}}_k^{1,m} = \frac{\Delta T}{24}\left(55\widehat{\mathscr{N}}_k^{1,m} - 59\widehat{\mathscr{N}}_k^{1,m-1} + 37\widehat{\mathscr{N}}_k^{1,m-2} - 9\widehat{\mathscr{N}}_k^{1,m-3}\right)$$

and similarly for $dN_k^{2,m}$.

Step 2: Apply AB4, AM6 or AM2* to determine changes in the linear terms.

(*a*) Compute $\widehat{\mathscr{L}}_k^{1,m} = \widehat{\mathscr{L}}_k^1(A^m, B^m)$, $\widehat{\mathscr{L}}_k^{2,m} = \widehat{\mathscr{L}}_k^2(A^m, B^m)$ using (4.6).

(*b*) Let $d\widehat{\mathscr{L}}_k^{1,m} =$

$$\begin{cases} \dfrac{\Delta T}{24}\left(55\widehat{\mathscr{L}}_k^{1,m} - 59\widehat{\mathscr{L}}_k^{1,m-1} + 37\widehat{\mathscr{L}}_k^{1,m-2} - 9\widehat{\mathscr{L}}_k^{1,m-3}\right), & |k| < k_1 \\ \dfrac{\Delta T}{1440}\left(475\widehat{\mathscr{L}}_k^{1,m} + 1427\widehat{\mathscr{L}}_k^{1,m} - 798\widehat{\mathscr{L}}_k^{1,m-1}\right. & \\ \qquad \left. + 482\widehat{\mathscr{L}}_k^{1,m-2} - 173\widehat{\mathscr{L}}_k^{1,m-3} + 27\widehat{\mathscr{L}}_k^{1,m-4}\right), & k_1 \leqslant |k| < k_2 \\ \dfrac{\Delta T}{4}\left(3\widehat{\mathscr{L}}_k^{1,m+1} - \widehat{\mathscr{L}}_k^{1,m-1}\right), & |k| \geqslant k_2 \end{cases}$$

and similarly for $d\widehat{\mathscr{L}}_k^{2,m}$.

Step 3: Compute the approximation $A^{m+1}(\xi_j)$ of $A(\xi_j, t_{m+1})$.

(*a*) Solve the system

$$\widehat{A}_k^{m+1} = \widehat{A}_k^m + d\widehat{\mathscr{N}}_k^{1,m} + d\widehat{\mathscr{L}}_k^{1,m}, \tag{4.8a}$$

$$\widehat{B}_k^{m+1} = \widehat{B}_k^m + d\widehat{\mathscr{N}}_k^{2,m} + d\widehat{\mathscr{L}}_k^{2,m} \tag{4.8b}$$

for $\widehat{A}_k^{m+1}$, $\widehat{B}_k^{m+1}$ by inverting a 2×2 linear system in the case $|k| \geqslant k_1$.

(*b*) Set $A^{m+1}(\xi_j) = F^{-1}(\widehat{A}_k^{m+1})$, and $B^{m+1}(\xi_j) = F^{-1}(\widehat{B}_k^{m+1})$.

Step 4: Filter the A_j^{m+1}, B_j^{m+1} as explained next, to prevent the dispersive tails colliding with the front of the respective waves through imposed periodicity.

4.2. *Filter*

In the cases of primary interest, the solution consists of two main waves that oscillate in leapfrog fashion as they propagate in the positive ξ direction. With each leap, some energy is shed behind the lead waves to form slowly moving dispersive tails. A generic snapshot at time T is shown in figure 5. Even though A and B correspond to waves on different pycnoclines, they are shown on the same axis, as in figure 4(*c*). The upper wave A is slightly behind the lower wave B, both followed by their small dispersive wave trains. Our goal is to solve for the evolution of the waves in an infinite domain. However, the imposed periodicity of the numerical method causes the dispersive wave trains to reenter the numerical domain at the right endpoint. To

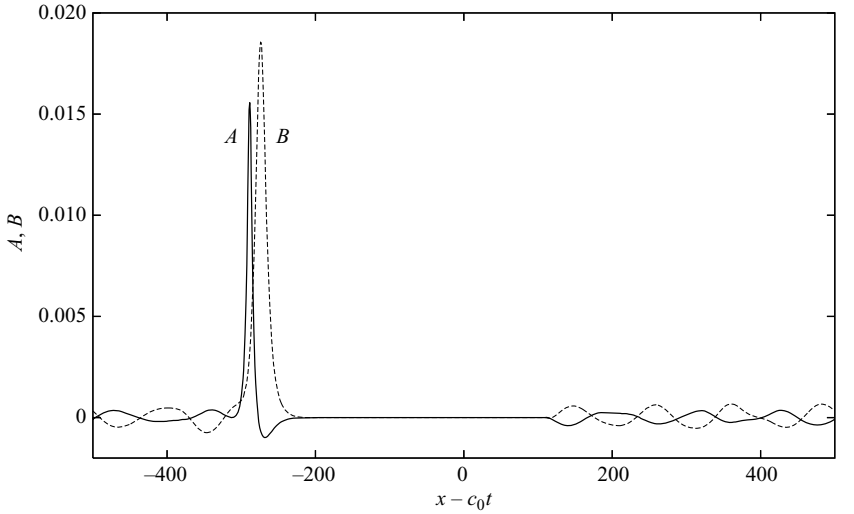

FIGURE 5. Snapshot of pycnocline disturbances $A(\xi, T)$ (solid) and $B(\xi, T)$ (dashed), where $\xi = x - c_0 t$, showing the region in front of the waves where the filter removes the dispersive tails.

prevent these slower moving tails from colliding with the fronts of the leapfrogging waves, a filter is applied: we first determine the average position x_{av} of the two waves and then filter the solution in a domain $[x_{av} - L_2, x_{av} - L_1]$ (mod L) by multiplying the solution by a linear function that decreases from 1 at $x_{av} - L_1$ to 0 at $x_{av} - L_2$. The domain is chosen to be sufficiently removed from the waves so that the filter does not affect the wave evolution. For example, if $L = 500$, such as in figure 5, we use $L_1 = 600$, $L_2 = 700$. For $L = 300$, we use $L_1 = 300$, $L_2 = 400$. This enables us to compute the primary wave motion until the waves separate to the extent that $|x_a - x_b| > 2L_1$, at which time the waves run into the filter and are removed by it. All the results shown herein remain unchanged if L, L_1 and $L_2 - L_1$ increase, and thereby we confirm that they are not affected by the filter.

4.3. *Input parameters*

As noted, the equations are non-dimensionalized using h_1, $\sqrt{h_1/g}$, and ρ_0 as length, time and density scales respectively. The remaining input parameters are A_0, B_0, h_2, and layer thicknesses H_j with corresponding densities ρ_j. Our normalization gives $h_1 = 1$ for the non-dimensional half-thickness of the upper pycnocline. The values of $h_{1,2}$ and ρ_j determine the unperturbed profile $\overline{\rho}(z)$, which in turn is used to compute the eigenfunctions $\phi_{1,2}$ and through them the values of $\alpha_{1,2}$, $\beta_{1,2}$ and $c_{1,2}$ that appear in (3.5).

In all computations we fix the non-dimensional parameters

$$H_1 = H_2 = H_3 = 15, \quad A_0 = B_0 = 0.5, \quad \rho_1 = 1.02, \quad h_1 = 1. \tag{4.9}$$

We study the dependence of the solution on the other three input parameters $\rho_{2,3}$ and h_2, which take on the following values:

$$h_2 = 1,\ 1.4,\ 1.8, \quad \rho_2 \in [1.05, 1.11], \quad \rho_3 \in [1.07,\ 1.22], \tag{4.10}$$

with the proviso that $\rho_3 > \rho_2 > \rho_1$ for static stability of the layered system. For each pycnocline centred at $z = z_0$ the unperturbed density distribution $\overline{\rho}(z)$ used to solve

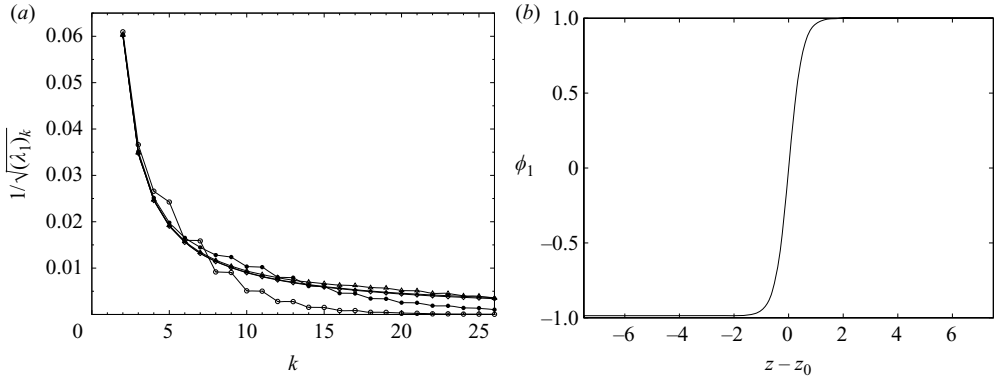

FIGURE 6. Solution of the eigenvalue problem (3.4) for the top pycnocline, with $\rho_1 = 1.02$, $\rho_2 = 1.05$, $h_1 = 1$, obtained using a finite difference approximation on a uniform mesh of N points. (*a*) The 25 largest values of $\sqrt{1/(\lambda_1)_k}$ for the non-zero eigenvalues $(\lambda_1)_k$, $k = 2, \ldots, 26$, with $N = 50$ (—○—), 100 (—●—), 200 (—△—), 400 (—▲—), 800 (—◇—). (*b*) Eigenfunction ϕ_1 corresponding to $(\lambda_1)_2$. The pycnocline is centred at $z = z_0$.

(3.3) and (3.4) is specified as

$$\overline{\rho}(z) = \frac{\rho_+ - \rho_-}{2} \tanh\left(\frac{2(z - z_0)}{h}\right) + \frac{\rho_+ + \rho_-}{2}, \quad -7.5 \leqslant z - z_0 \leqslant 7.5, \tag{4.11}$$

where h is the pycnocline half-thickness and ρ_+ and ρ_- are the fluid densities above and below the pycnocline, respectively. Note that this density profile is constant to within 3.5 % of ρ_+, ρ_- outside of the middle layer of thickness $2h$. The eigenvalue problem (3.4) is solved on the interval $z \in I = [z_0 - 7.5, z_0 + 7.5]$ by approximating the equation on a uniform grid using second-order finite differences and specifying the boundary conditions at $z = z_0 + 7.5$ for ϕ_1 and at $z = z_0 - 7.5$ for ϕ_2. (Here, the precise length of the interval I, in this case 15, is not important, as long as I includes the region in which $\overline{\rho}$ varies significantly.) The resulting finite dimensional eigenvalue problem is solved using Matlab.

The wave speeds $c_{1,2}$ and eigenfunctions $\phi_{1,2}$ are determined to be those corresponding to the smallest non-zero eigenvalues, $(\lambda_{1,2})_2 = 1/c_{1,2}^2$. Note that $(\lambda_{1,2})_1 = 0$ is an eigenvalue of the system corresponding to constant eigenfunctions $\phi_{1,2} = 1$, which is commonly referred to as the mode-1 eigenfunction. However, as explained earlier, in our asymptotic system this eigenvalue corresponds to infinite speeds $c_{1,2} = 1/(\lambda_{1,2})_1$, and so these modes are excluded here. The smallest non-zero eigenvalue corresponds to the mode-2 eigenfunction and is denoted here by subscript 2. As an example, figure 6(*a*) shows the 25 largest values of $\sqrt{1/(\lambda_1)_k}$ for the non-zero eigenvalues $(\lambda_1)_k$, $k = 2, \ldots, 26$, corresponding to $\rho_1 = 1.02$, $\rho_2 = 1.05$, $h_1 = 1$, computed using a uniform mesh of N points, with N varying between 50 and 800, as indicated in the caption. The figure shows that these values converge as N increases. The largest converges to $c_1 = \sqrt{1/(\lambda_1)_2} = 0.0602$ to within three significant digits. The mode-2 eigenfunction ϕ_1 corresponding to the eigenvalue $(\lambda_1)_2$ is shown in figure 6(*b*). The values of α_1 and β_1 computed from ϕ_1 converge to 2.38 and 0.0116, respectively, to within three significant digits.

The parameters $\alpha_{1,2}$ and $\beta_{1,2}$ are obtained by integrating the eigenfunctions $\phi_{1,2}$ over the interval I numerically, using the trapezoidal rule. The process is repeated with different resolutions (using $N = 50$, 100, 200, 400 points) giving an indication of the

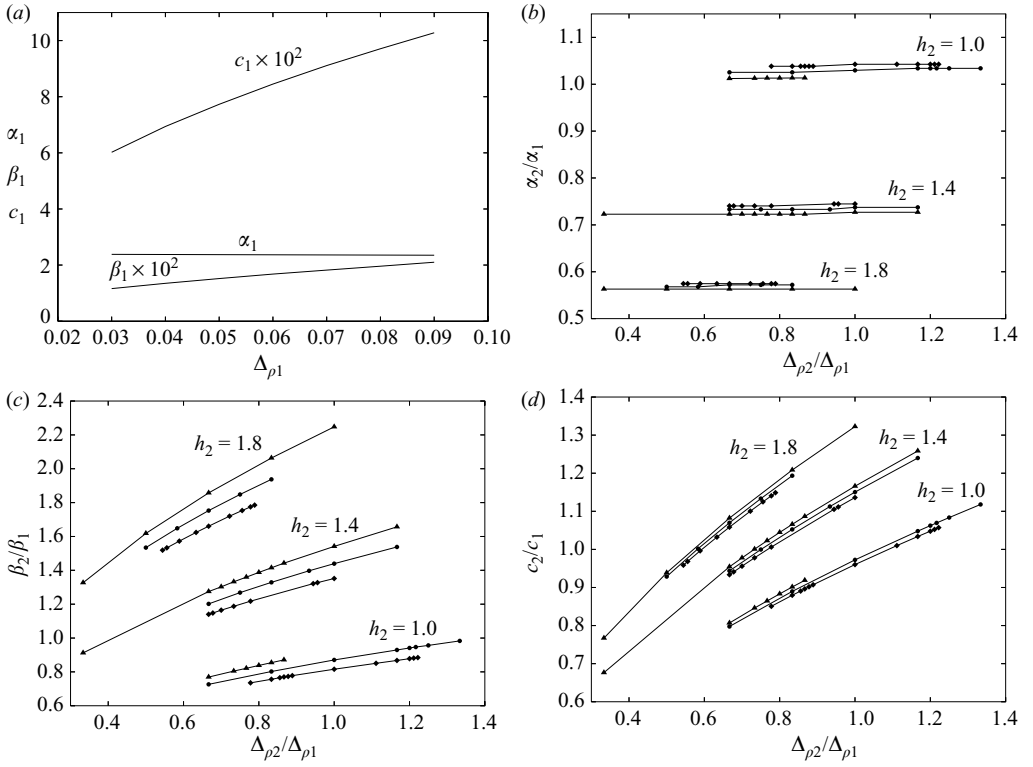

FIGURE 7. (*a*) Values of α_1, β_1 and c_1 on the upper pycnocline as a function of the density jump $\Delta\rho_1$. (*b–d*) Ratio of the nonlinear coefficients α_2/α_1, β_2/β_1 and linear wave speeds c_2/c_1 as a function of $\Delta\rho_2/\Delta\rho_1$, for the indicated values of h_2 and $\Delta\rho_1 = 0.03$ (—○—), $\Delta\rho_1 = 0.06$ (—△—), $\Delta\rho_1 = 0.09$ (—◆—).

accuracy obtained. This method differs from the work of Liu *et al.* (1980), who used approximate formulas for $\alpha_{1,2}$, $\beta_{1,2}$ and $c_{1,2}$. Figure 7 shows the parameters computed for a range of dimensionless values of $\Delta\rho_1 = \rho_2 - \rho_1$, $\Delta\rho_2 = \rho_3 - \rho_2$. Figure 7(*a*) shows how the upper pycnocline parameters α_1, β_1 and c_1 vary with $\Delta\rho_1$. Figure 7(*b–d*) show how the lower pycnocline parameters α_2, β_2 and c_2 vary with $\Delta\rho_2$; note that the $\Delta\rho_2/\Delta\rho_1$ scaling nicely groups these data according to the values of h_2 in each case.

The solid symbols in figure 7 denote the parameter values computed using the finite difference approximation described above. The solid curves are piecewise linear interpolants. For the results plotted later in figure 18, we computed the above parameters on a fine grid of density jumps and then obtained smoothed curves using polynomial least-squares approximations. This was done in order to avoid variations and jumps introduced by the finite difference approximation error when $\Delta\rho$ is changed by a very small amount.

4.4. *Numerical parameters and runtime*

The results shown in § 5 were performed using $N = 2048$, $L = 500$ and ΔT sufficiently small for stability and accuracy. The values of ΔT ranged from 0.1 down to 0.00025. All results shown herein have converged under mesh refinement. To ensure this, several of the cases shown were computed using $N = 1024$, 2048 and 4096 and sufficiently small ΔT. It was confirmed that the quantities reported, including number

of oscillations, separation time, separation speed and maximal amplitudes remain unchanged under such mesh refinement to within several digits of precision. It was also confirmed that the values of the filter parameters L, L_1 and L_2 used where sufficiently large to not affect the results. A further measure of numerical accuracy is the extent to which the total energy is conserved. This is addresssed later in § 5.1.2.

All computations were performed on a personal computer with an AMD Athlon 1.2 Ghz processor. For $N = 2048$, the elapsed time was 32 s for 10,000 time steps, leading to total execution times of 1 hr to 21 days.

5. Presentation of results

5.1. *Oscillating solutions*

Liu *et al.* (1980) solved the governing equations numerically for one set of parameters α, β, c and found the leapfrogging behaviour, although they were only able to compute 3 hops. In the laboratory experiments of Weidman & Johnson (1982) performed in a 10 m tank viscous damping precluded data acquisition over more than 3 clean hops. The results presented here are not limited by viscous damping effects manifest in a laboratory experiment and we have overcome the difficulties of long-time numerical integrations.

Guided by the experimental results of Weidman & Johnson (1982) and the numerical results of Liu *et al.* (1980), we find a range of input parameters $\rho_{1,2,3}$ and $h_{1,2}$ for which the numerical solution oscillates in leapfrog fashion. All the oscillating solutions have the same generic characteristics. In this section we describe sample leapfrog solutions in detail, and evaluate the accuracy with which the numerical method conserves energy.

5.1.1. *A sample solution*

The choice $\rho_1 = 1.02$, $\rho_2 = 1.11$, $\rho_3 = 1.19$, $h_1 = 1$ and $h_2 = 1$ illustrates the generic features well and at a scale easily shown in print. The corresponding pycnocline parameters, computed as described in § 4.3, are $\alpha_1 = 2.35$, $\alpha_2 = 2.44$, $\beta_1 = 0.657\tau$, $\beta_2 = 0.511\tau$, $c_1 = 3.219\tau$ and $c_2 = 2.920\tau$, where $\tau = 1/\sqrt{980}$. These are non-dimensional values, as are all results presented in this paper. However, the computations were performed using the dimensional equations of motion, which is the reason for the appearance of the factor τ above and the resulting unusual non-dimensional times given below.

Equations (3.5) with the given input parameters were solved up to time $T = 35000/\tau \approx 110 \times 10^4$ using numerical parameters $N = 2048$, $L = 300$, $\Delta T = 0.025/\tau \approx 0.783$. With these values the solution has converged, meaning that the results remain unchanged to within several digits if N, L, L_1 and $L_2 - L_1$ are increased or ΔT is decreased.

Figure 8 shows the computed solution $A(\xi, T)$ (solid) and $B(\xi, T)$ (dashed) as a function of $\xi = x - c_0 t$ at the times $0 \leqslant T \leqslant 10.174 \times 10^4$, as indicated. At $T = 0$, the waves A and B are identical, given by the Joseph solitary wave (3.8) with amplitude $A_0 = B_0 = 0.5$ and $h_2 = h_1 = 1$. For $T > 0$, both waves slowly travel to the right, slightly faster than the average linear speed c_0. As they propagate, their spatial separation oscillates in time. Initially, wave A travels faster, and is ahead of wave B at $T = 0.783 \times 10^4$. Then B travels faster and is ahead of A at the next time shown $T = 1.565 \times 10^4$. This process repeats itself, albeit with increasing oscillation period. For example, in the last three frames shown, it takes approximately twice as much time for B to hop past A compared to the first hop. The figure indicates that

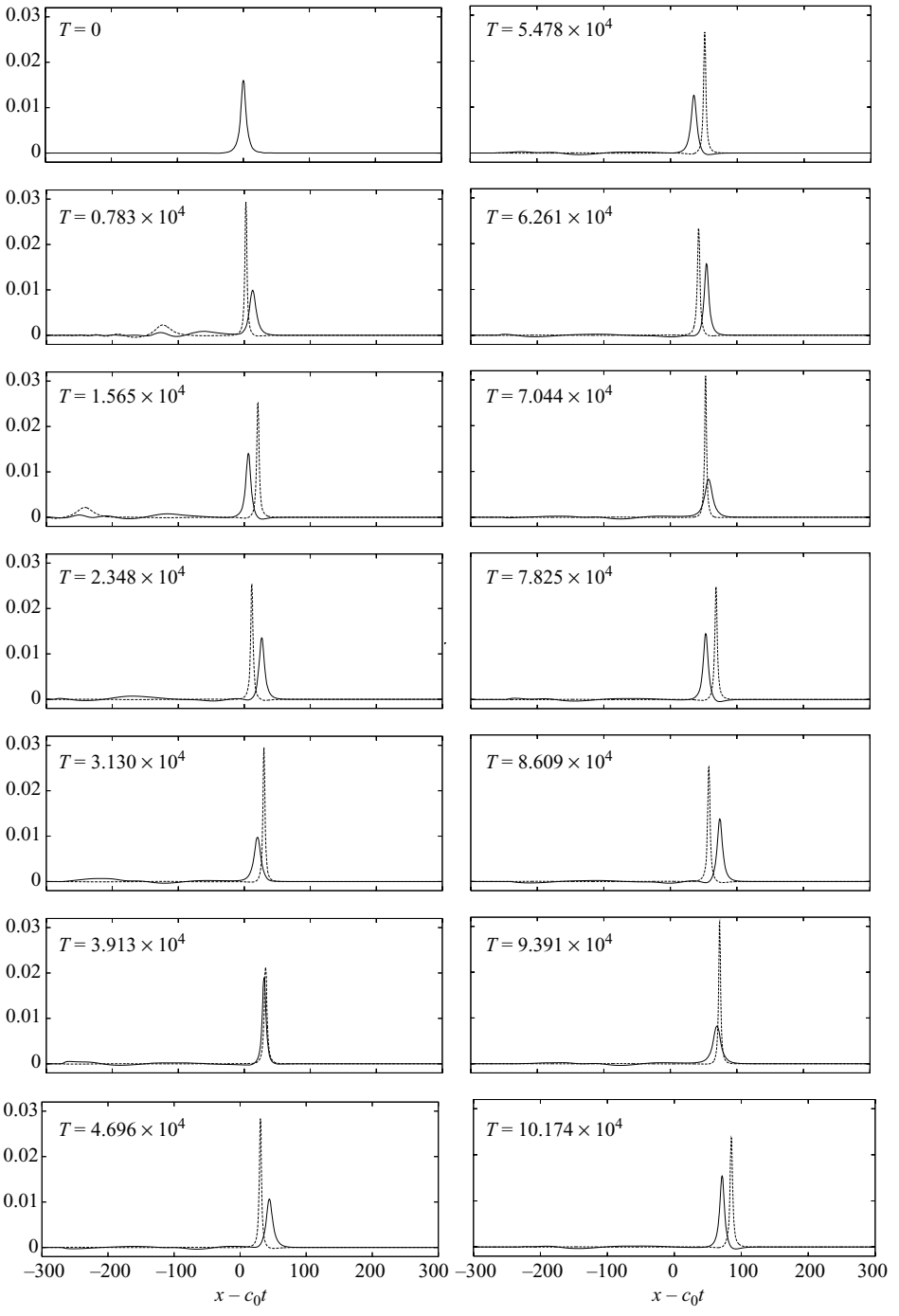

FIGURE 8. Upper and lower pycnocline amplitudes $A(\xi, T)$ (solid) and $B(\xi, T)$ (dashed) as a function of $\xi = x - c_o t$ at equal time intervals in the range $0 \leqslant T \leqslant 10.174 \times 10^4$, as indicated, where $\rho_1 = 1.02$, $\rho_2 = 1.11$, $\rho_3 = 1.19$ and $h_2 = h_1 = 1$.

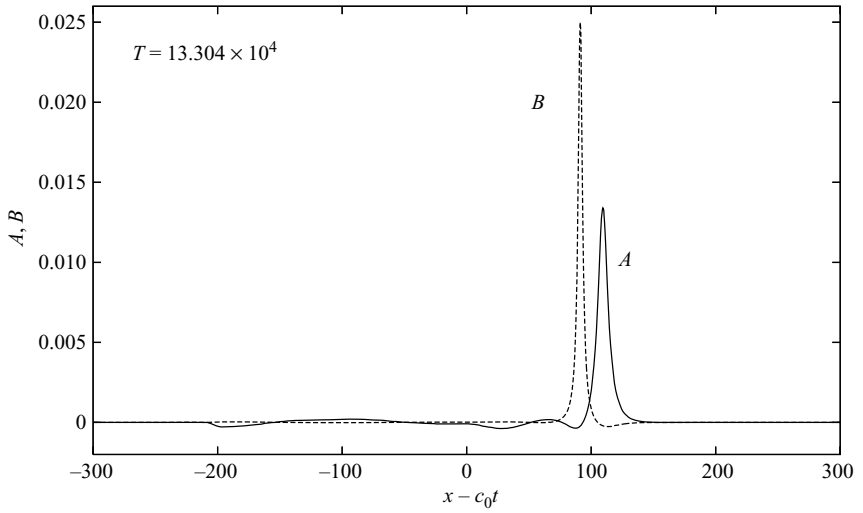

FIGURE 9. Closeup of the amplitudes $A(\xi, T)$ and $B(\xi, T)$ as a function of $\xi = x - c_0 t$ at the indicated time, where $\rho_{1,2,3}$ and $h_{1,2}$ are as in figure 8.

even though the peak amplitude of A is always smaller than that of B, both peak amplitudes oscillate as well. The details of this oscillation, which is a leapfrogging motion as observed in Weidman & Johnson (1982), will be discussed later in § 5.1.3.

As the waves propagate they shed energy downstream. Initially, at time $T \leqslant T_0 = 500/\tau (\approx 1.565 \times 10^4)$, the lead waves shed relatively large disturbances downstream. This initial time period is a transient interval in which the waves adjust to a slowly varying oscillatory state. At later times, in the slowly varying oscillating state, the amount of energy shed downstream is small, albeit non-zero. The closeup in figure 9 shows the dispersive wavetrain in finer detail. The small energy release is similar to that observed by Wright & Scheel (2007) in a case of nonlinearly coupled KdV waves.

The downstream release of energy by the waves is responsible for the slow increase in the oscillation period, and in the maximal separation distance within a period. Eventually the separation distance increases past a critical value and the waves separate as independent, non-interacting solitary waves on their respective pycnoclines. This can be seen in figure 10, which shows the solution for $57.91 \times 10^4 \leqslant T \leqslant 72.00 \times 10^4$. In this example, the waves exchange positions one last time at $T = 58.10 \times 10^4$, placing the A wave in the front. After this time, the faster moving A wave remains forever in front, and the two waves separate at constant speed. We denote the time $T_s = 58.10 \times 10^4$ as the *separation time*. The closeup in figure 11 at $T = 78.262 \times 10^4 > T_s$ shows that, after separation, energy is no longer released downstream and the waves travel as independent solitary waves.

The evolution of the peak wave amplitudes

$$A_m(T) = \max_{\xi} A(\xi, T), \quad B_m(T) = \max_{\xi} B(\xi, T) \tag{5.1}$$

during the leapfrog process is displayed in figure 12(a). Clearly, both A_m and B_m oscillate about their mean values, but with a larger swing on each pass, and with an oscillation period that increases in time. At $T > T_s$ the oscillations stop whilst A_m, B_m rapidly approach their final constant values.

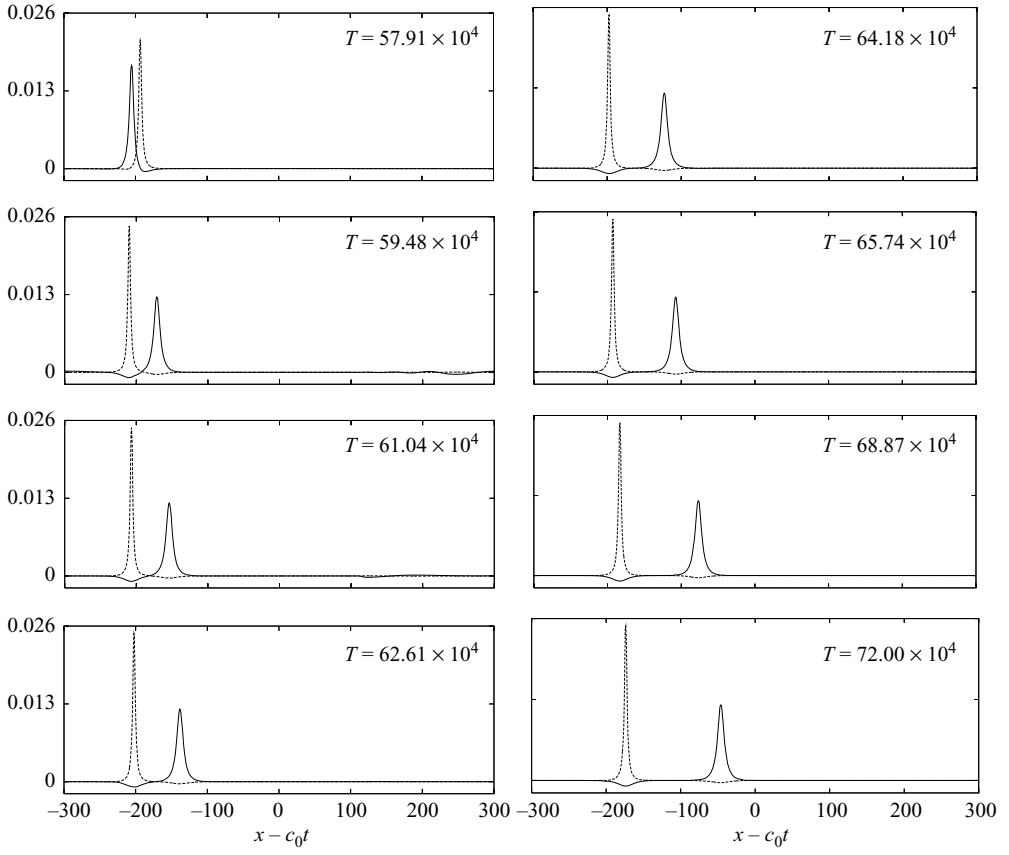

FIGURE 10. Amplitudes $A(\xi, T)$ and $B(\xi, T)$ as a function of $\xi = x - c_0 t$ at the indicated times, where $\rho_{1,2,3}$ and $h_{1,2}$ are as in figure 8. Incipient wave separation occurs at $T = T_s = 58.096 \times 10^4$.

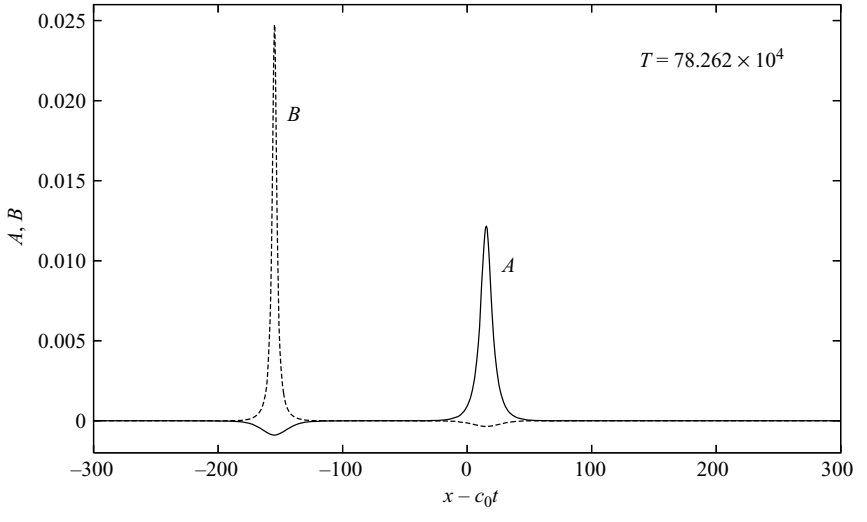

FIGURE 11. Closeup of the amplitudes $A(\xi, T)$ and $B(\xi, T)$ as a function of $\xi = x - c_0 t$ at the indicated time, where $\rho_{1,2,3}$ and $h_{1,2}$ are as in figure 8.

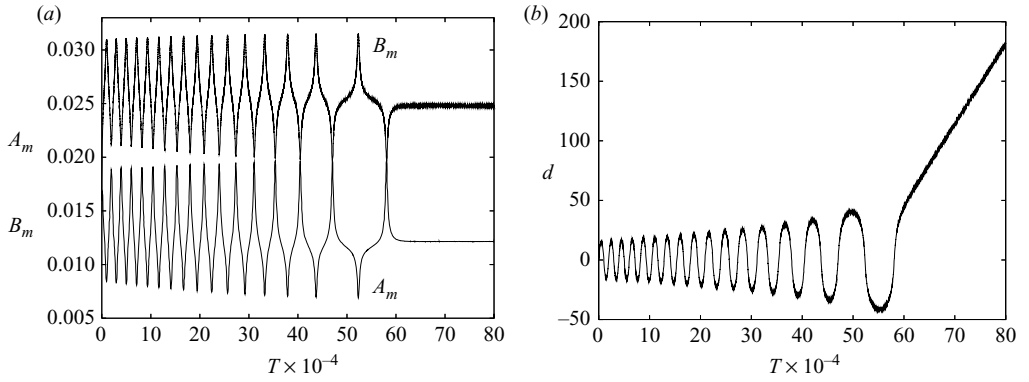

FIGURE 12. (*a*) Maxima $A_m(T)$, $B_m(T)$, as indicated. (*b*) Separation distance $d(T)$, where $\rho_{1,2,3}$ and $h_{1,2}$ are as in figure 8.

Figure 12(*b*) shows the evolution of the wave separation distance d, defined to be the signed distance between $A_m(T)$ and $B_m(T)$, *viz.*

$$d(T) = \xi_a(T) - \xi_b(T), \quad \text{where} \quad A(\xi_a(T), T) = A_m(T), \quad B(\xi_b(T), T) = B_m(T) \tag{5.2}$$

as it evolves in time. With this definition, the separation distance is positive when A is ahead of B, negative when B is ahead of A and passes through zero when the waves cross. The figure clearly shows that the spatial separation oscillates, and that both the oscillation amplitude and period slowly increase until the waves permanently separate. The separation time T_s is the last time at which $d = 0$. Subsequently, each wave travels with constant velocity and the separation distance increases linearly in space and time.

5.1.2. *Conservation of energy*

The governing equations conserve the total energy

$$E(T) = \frac{1}{2}\int_{-\infty}^{\infty} \boldsymbol{u}\cdot\boldsymbol{u}\ \mathrm{d}\xi = \frac{1}{2}\int_{-\infty}^{\infty}\left(\frac{A^2(\xi,T)}{\beta_1} + \frac{B^2(\xi,T)}{\beta_2}\right)\ \mathrm{d}\xi, \tag{5.3}$$

where $\boldsymbol{u}(\xi, T) = [A(\xi, T)/\sqrt{\beta_1},\ B(\xi, T)/\sqrt{\beta_2}]$. Note that although we have called E the energy of the system since it is conserved for solutions of (3.5), it is not exactly the same as the total energy of the original physical system, although it is an asymptotic approximation to this. To determine the extent to which the numerical method conserves energy, we view the algorithm as a two-step method. First, the solution is advanced using the pseudo-spectral scheme, then the filter is applied to remove the tail of the dispersive trailing waves,

$$\boldsymbol{u}_n^* = \boldsymbol{u}_n + \Delta T M(\boldsymbol{u}_n), \quad \boldsymbol{u}_{n+1} = F(\boldsymbol{u}_n^*), \tag{5.4}$$

where the subscript n denotes evaluation at T_n. Here M is the pseudo-spectral scheme used to advance $\boldsymbol{u}$, and F denotes the action of the filter. The filter removes energy from the system and therefore the energy in the computational domain

$$E_c(T_n) = \frac{1}{2}\int_{-L}^{L} \boldsymbol{u}_n\cdot\boldsymbol{u}_n\,\mathrm{d}\xi \tag{5.5}$$

is not conserved. The question is to what extent the pseudo-spectral scheme conserves energy. Since the filter acts on the distant waves and was confirmed not to affect the

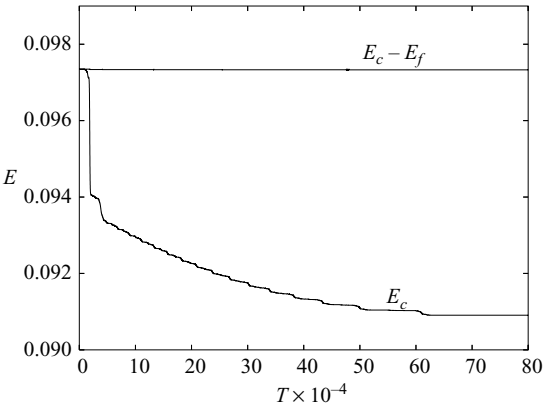

FIGURE 13. Energy in computational domain $E_c(T)$, and energy $E_m(T) = E_c(T) - E_f(T)$ obtained after removing loss due to filter, where $\rho_{1,2,3}$ and $h_{1,2}$ are as in figure 8.

motion of the interacting primary waves, energy conservation of the pseudo-spectral scheme would give an indication of the accuracy of the latter.

The energy lost at time T_n due to the filter is

$$E_f(T_n) = \sum_{j=1}^{n-1} \int_{-L}^{L} \left[F(\boldsymbol{u}_j^*) \cdot F(\boldsymbol{u}_j^*) - \boldsymbol{u}_j^* \cdot \boldsymbol{u}_j^* \right] \mathrm{d}\xi. \tag{5.6}$$

The energy lost due to the pseudo-spectral scheme is

$$E_m(T_n) = E_c(T_n) - E_f(T_n)\ . \tag{5.7}$$

The extent to which E_m decays indicates the extent to which the scheme is not energy conserving. To find E_m we compute E_c and E_f from (5.5) and (5.6) using the trapezoid rule for all integrations.

Figure 13 shows the evolution of $E_c(T)$ in the computational domain and $E_m(T) = E_c - E_f$ obtained after removing the effect of the filter. E_c decreases from 0.09735 at $T = 0$ to 0.09091 at $T = 80 \times 10^4$, which is a loss of 6.6 % from the starting value. The decrease is relatively large for $T \leqslant 3.1 \times 10^4$, in the initial transient when large waves are shed. At later times in the slowly varying state the decrease is more gradual. At large times, after the waves separate and no more energy is shed downstream, the filter is inactive and the total energy remains approximately constant.

While E_c decreases by 6.6 % from the starting value, E_m remains almost constant, decreasing by less than 0.008 % over the entire time interval of the computation. This shows that the filter is responsible for the bulk of the energy loss. This is consistent with the fact that after separation $T > T_s = 58.10 \times 10^4$, when the filter is inactive, the total energy E_c stays constant within 0.001 %. We conclude that the pseudo-spectral method conserves the total energy to within 0.008 % in the time interval shown.

5.1.3. *Details on the leapfrogging oscillation*

Details of the leapfrogging scenario are here displayed using the new set of parameters $\rho_1 = 1.02$, $\rho_2 = 1.11$, $\rho_3 = 1.167$, $h_1 = 1$, $h_2 = 1.8$ with corresponding values $\alpha_1 = 2.35$, $\alpha_2 = 1.35$, $\beta_1 = 0.657\tau$, $\beta_2 = 1.067\tau$, $c_1 = 3.219\tau$, $c_2 = 3.323\tau$, where, as before, $\tau = 1/\sqrt{980}$ is the scaling parameter that arises in non-dimensionalizing the results. The solution for these parameters, displayed over one period of leapfrog

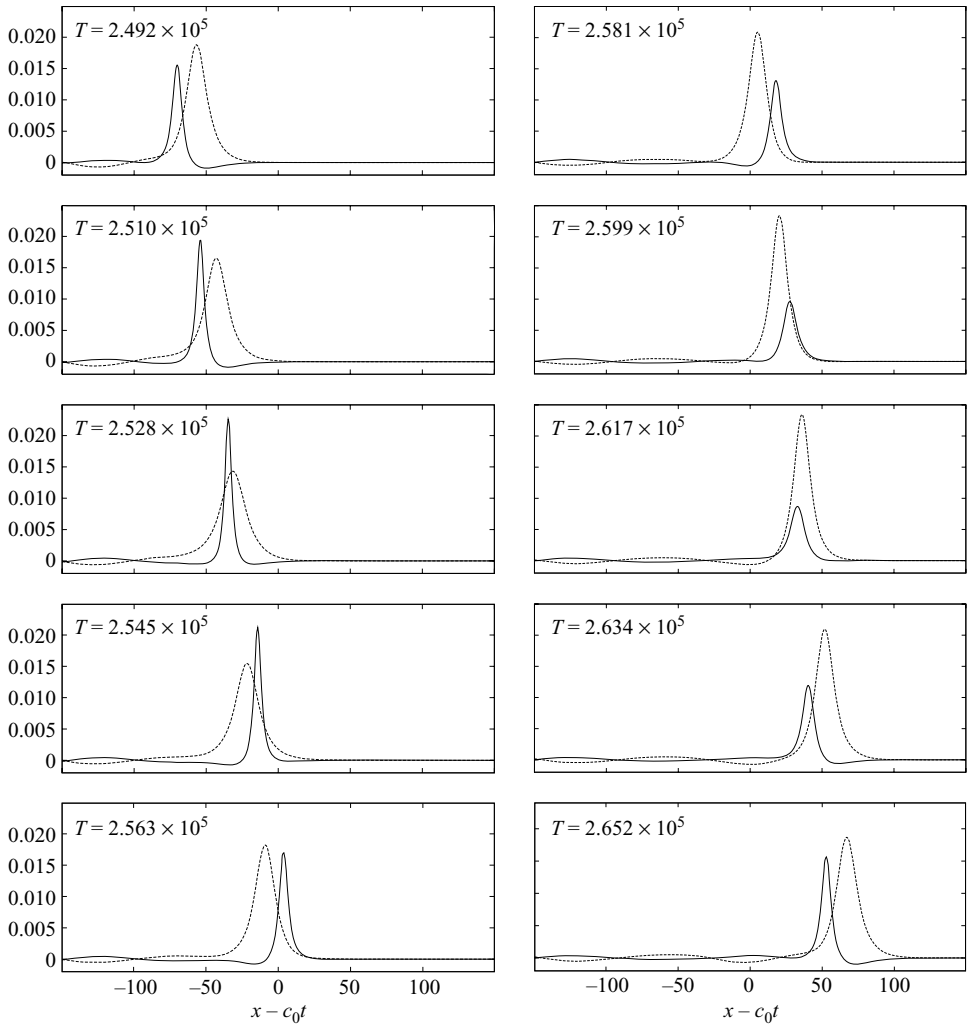

FIGURE 14. Amplitudes $A(\xi, T)$ and $B(\xi, T)$ as a function of $\xi = x - c_0 t$ at the indicated times, where $\rho_1 = 1.02$, $\rho_2 = 1.11$, $\rho_3 = 1.167$ and $h_1 = 1$, $h_2 = 1.8$.

oscillation in figure 14, nicely illustrates the evolution of the trailing tails and the interaction between the leapfrogging waves.

Initially ($T = 2.492 \times 10^5$) the B wave on the lower pycnocline leads the A wave on the upper pycnocline. Energy is transferred backwards to the A wave which grows in amplitude ($T = 2.510 \times 10^5$), accelerates ($T = 2.528 \times 10^5$) and moves ahead of the B wave ($T = 2.545 \times 10^5$). Meanwhile, the B wave has decreased in amplitude. The process repeats itself with the role of A and B reversed until, at $T = 2.652 \times 10^5$, the two waves are in their same relative position, but with slightly diminished amplitudes.

This describes the leapfrog oscillation as observed and described in Weidman & Johnson (1982). Further details of the interaction and the energy release into the tail can be obtained from these computations. For example, it is clear that the tails in figure 14 consist of travelling sinusoidal waves, generated in the wake of the primary waves. Comparing the first and last frames of figure 14 shows that over one period

of leapfrog oscillation, exactly one full trailing wavelength is produced behind each primary wave.

In more detail we see that each A, B elevation wave is accompanied by a phase-locked depression in the B, A field, respectively. This is most clearly seen for the wider B wave, and when the two waves are well separated. For instance in the first panel in figure 14 the signature of the leading B wave on its neighbouring pycnocline is seen as a distinct depression just upstream of the primary A wave. When the B wave starts drifting to backwards relative to the A wave ($T = 2.545 \times 10^5$), one observes the emergence of both a depression at the rear of the A wave and an elevation wave at the rear of the B wave. When the leapfrogging oscillation is half-way completed ($T = 2.581 \times 10^5$), with the B wave now trailing the A wave, we see that the radiated waves have moved further to the left, and the phase-locked depression signature of the B wave is again clearly visible, distinct from the radiated wave immediately downstream. The cycle is then completed as the B wave accelerates to again overtake the A wave.

Next we present a possible interpretation of these numerical results, based on the theoretical analysis of Wright & Scheel (2007) for a coupled KdV system, and on an asymptotic model we will describe in § 6 below. The evolution equations (3.1*a*,*b*) are assumed to support *exact* steady solitary waves, that is A, $B = A_s(Y)$, $B_s(Y)$, where $Y = \xi - VT$. Note that there is an A- and a B-component for each such solitary wave. Our interest is in the case when there are two such solitary waves $A_s^{1,2}$, $B_s^{1,2}$ with speeds $V_{1,2}$ such that $V_1 \approx V_2$. We assume that one of these waves is an elevation wave on the upper pycnocline, $A_s^1 > 0$, and has a *small* signature depression wave $B_s^1 < 0$ on the lower pycocline. The other wave is reversed, that is, it is an elevation wave on the lower pycnocline, $B_s^1 > 0$, and has a *small* signature of depression $A_s^1 < 0$ on the upper pycocline. These assumptions are supported by our numerical simulations of separated solitary waves (see, for instance, figures 10 and 11).

Leapfrogging occurs when these waves are slightly perturbed. In § 6 we develop an asymptotic model to analyse this situation, and show that the interaction between the two waves can be described by a certain second-order ordinary differential equation (6.17) for their separation distance P. When the constant in (6.17) is positive, that is $\Omega^2 > 0$ where

$$\Omega^2 = -\frac{\pi^4 m_1 m_2 \beta_1 \beta_2}{2H_2^4 \alpha_1 \alpha_2} \left[\alpha_1^2 \left(\frac{\rho_3}{\rho_2} + m_2^2 \right) + \alpha_2^2 \left(\frac{\rho_1}{\rho_2} + m_1^2 \right) \right], \tag{5.8}$$

then the model is neutrally stable and sustains leapfrogging solutions. The linear result, which agrees with results of Liu *et al.* (1982), is that in this case the two waves oscillate back and forth with an approximate frequency Ω.

Note that for all our computations $\alpha_{1,2} > 0$, $\beta_{1,2} > 0$, $m_1 m_2 < 0$, so indeed $\Omega^2 > 0$. Using the system parameter values for the results shown in figure 8, we find from (5.8) that $\Omega = 0.036\tau$, giving the oscillation period $2\pi/\Omega = 175/\tau = 5.5 \times 10^3$. The numerical results show that the leapfrogging period in the early stages is about 2×10^4. A similar comparison can be made for the results shown in figure 13, where $\Omega = 0.056\tau$, and the numerically observed period is about 1.5×10^4. In both cases the numerical period is considerably (3.6 and 4.3 times) longer than the linear prediction.

The explanation for this discrepancy is addressed in § 6. There, we show that our asymptotic model predicts a family of periodic solutions, and only those with the smallest separation distances P and velocity differences Q will have frequencies Ω. As either P or Q increases, so does the oscillation period due to nonlinearity, up to limiting values corresponding to an infinite period. The model shows that even for

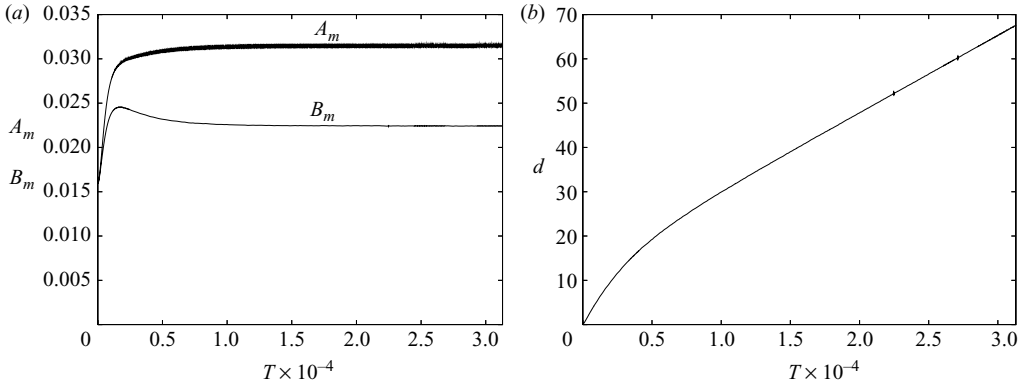

FIGURE 15. (*a*) Maxima $A_m(T)$, $B_m(T)$, as indicated. (*b*) Separation distance $d(T)$, where $\rho_1 = 1.02$, $\rho_2 = 1.05$, $\rho_3 = 1.0735$ and $h_2 = h_1 = 1$.

zero initial separation distance, if the initial velocity difference is too large, then the waves separate immediately, without incurring any leapfrog oscillation. This aspect is explored in § 5.2.

The numerical simulations in figure 14 furthermore show that essentially one component of the radiating wave field is produced on each cycle of leapfrog oscillation. That is, the frequency of the radiating waves is the same as the oscillation frequency, which would equal Ω if P, Q were small. In § 6 we explore the destabilizing effect of the radiating waves on the periodic solutions, causing the oscillation period and amplitude to increase. A more delicate analysis is needed to determine the amplitude of the radiating waves at their point of generation, and we shall not pursue that aspect further in this paper.

5.2. *Immediate separation*

For a range of input parameters $\rho_{1,2,3}$ and h_2, the solution does not oscillate, but instead the two waves immediately separate. Figure 15 shows results for one such a case, using $\rho_1 = 1.02$, $\rho_2 = 1.05$, $\rho_3 = 1.0735$ and $h_1 = h_2 = 1$. Figure 15(*a*) shows that the maximum amplitudes A_m and B_m quickly approach a constant value without undergoing any oscillation. The evolution of the separation distance d in figure 15(*b*) is devoid of oscillation and quickly approaches linear growth as the waves spatially separate. In the oscillatory case, on the other hand, the separation distance quickly departs from linear growth to reach a local maximum (see e.g. figure 12*b*). That is, the curvature of $d(T)$ differs markedly between the two cases, making it easy to distinguish early on whether a set of parameters will lead to oscillation or separation. In the following section we explore the range of parameters for which leapfrog oscillations are possible.

5.3. *Parameter study*

5.3.1. *Parameter space of oscillations*

To determine the region in the parameter space where leapfrog oscillations are obtained, we computed results for a range of values of $\Delta\rho_1$, $\Delta\rho_2$, for each of $h_2 = 1.0$, 1.4, 1.8, keeping $\rho_1 = 1.02$ and $h_1 = 1$ fixed. For each case solutions were computed until it could be clearly established from the maximum amplitudes and the separation distance whether the solution would oscillate or not. The results are summarized in figure 16. Figures 16(*a*, *d*), 16(*b*, *e*), 16(*c*, *f*) correspond to $h_2 = 1$, 1.4, 1.8, respectively. Figure 16(*a–c*) show the values of $h_2\Delta\rho_2$ used, figure 16(*d–f*) show the corresponding

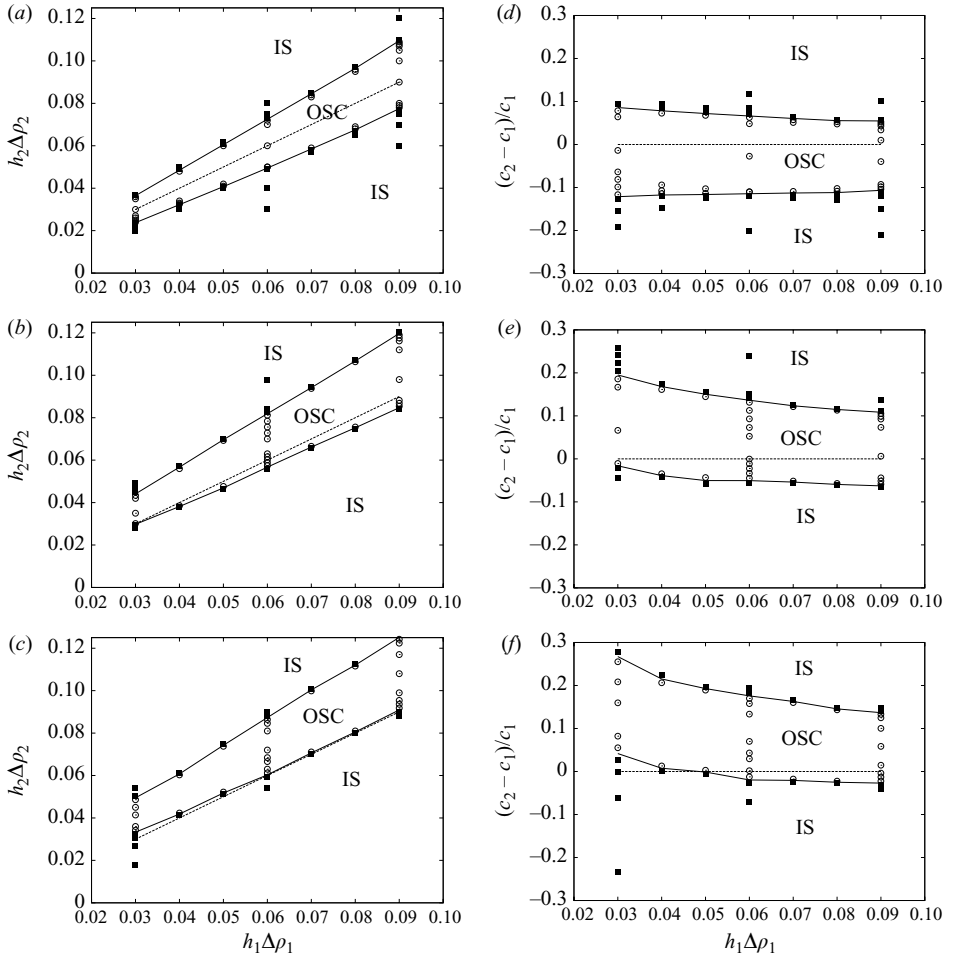

FIGURE 16. Values of parameters $h_2\Delta\rho_2$ (*a–c*) and $(c_2 - c_1)/c_1$ (*d–f*) as a function of $h_1\Delta\rho_1$ for which the chosen initial conditions lead to oscillations (open circles) or immediate wave separation (solid squares). In all cases, $h_1 = 1$, $\rho_1 = 1.02$. (*a*, *d*) $h_2 = 1.0$, (*b*, *e*) $h_2 = 1.4$ and (*c*, *f*) $h_2 = 1.8$. The solid curves denotes the boundary separating the two regions. Thus in the region between the curves (labelled OSC) leapfrog oscillations occur, and elsewhere (labelled IS) there is immediate separation. The dashed line denotes the points with $h_1\Delta\rho_1 = h_2\Delta\rho_2$ (*a–c*) and with $c_1 = c_2$ (*d–f*).

values of $(c_2 - c_1)/c_1$, all as functions of $h_1\Delta\rho_1$. The data points for which the waves immediately separate are shown as solid squares, and the ones for which there is at least one oscillation are shown as open circles. The boundary between the circles and the squares is approximated by solid curves. Many data points were collected near this boundary in order to resolve it well. Thus, we find a connected region in the parameter space lying in between the solid curves, labelled OSC in the figure, corresponding to oscillating solutions. The remaining region, labelled IS, corresponds to immediately separating solutions. In the upper IS region, where $\Delta\rho_2$ is relatively large, the upper wave travels slower than the lower wave, whereas in the lower IS region, the upper wave travels faster than the lower wave.

As a reference, the line $h_1\Delta\rho_1 = h_2\Delta\rho_2$ is also plotted in figure 16(*a–c*), and the line $c_1 = c_2$ is plotted in figure 16(*d–f*). For $h_2 = 1$ (figure 16*a*,*d*) the region of oscillation is

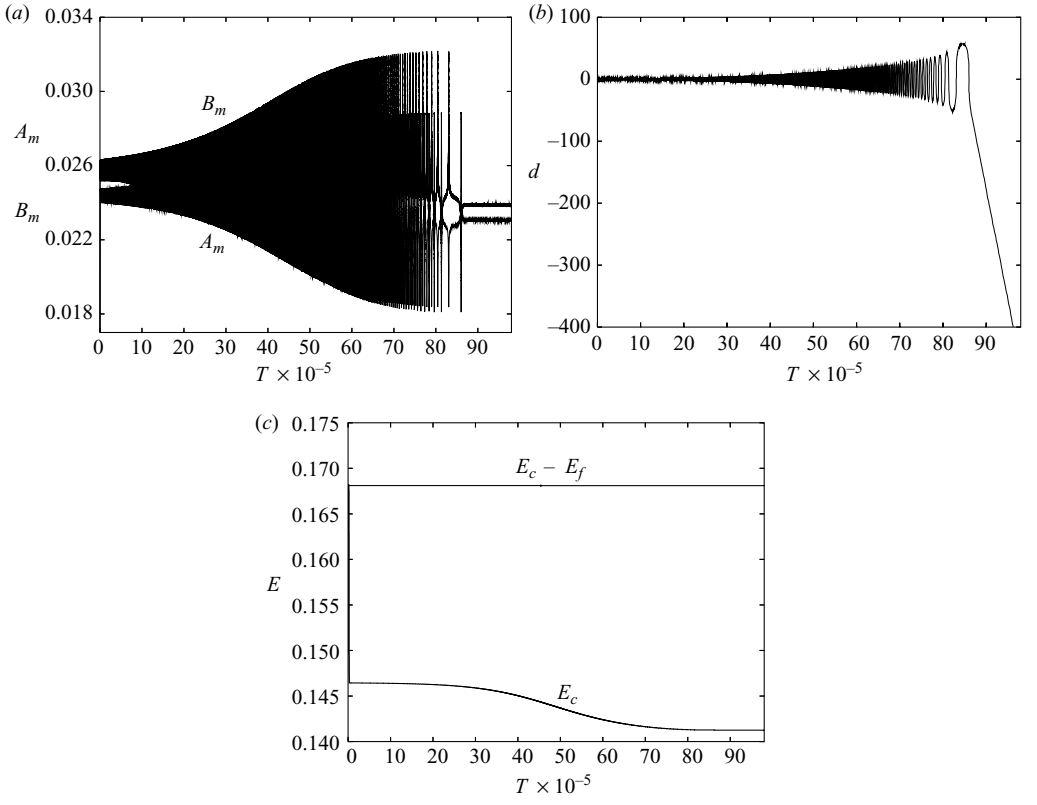

FIGURE 17. (*a*) Maxima $A_m(T)$, $B_m(T)$; (*b*) separation distance $d(T)$; (*c*) energy $E_c(T)$ and $E_m(T) = E_c(T) - E_f(T)$. Here, $\rho_1 = 1.02$, $\rho_2 = 1.05$, $\rho_3 = 1.076$ and $h_1 = 1, h_2 = 1.4$.

approximately centred about this line. That is, oscillations occur when $\Delta\rho_1$, the density jump across the upper pycnocline, is approximately equal to $\Delta\rho_2$, the density jump across the lower pycnocline, and when the two phase speeds are also approximately equal. For larger lower pycnocline thicknesses $h_2 = 1.4$ and 1.8, the region of leapfrog oscillation shifts slightly upwards with oscillations occurring only if $h_2\Delta\rho_2$ and c_2 are relatively large compared to $h_1\Delta\rho_1$ and c_1 respectively.

While one may argue that these results depend on the chosen initial condition, they show that there is a relatively small region near $\Delta\rho_1 = \Delta\rho_2$ for which oscillatory motion exists.

5.3.2. *Another sample solution*

To show the extent to which the oscillatory solutions presented in § 5.1 are generic, we present another oscillatory solution. The evolution of maximum wave amplitudes and separation distance for $\rho_1 = 1.02$, $\rho_2 = 1.05$, $\rho_3 = 1.076$ with $h_1 = 1$ and $h_2 = 1.4$ are plotted in figure 17(*a*, *b*), respectively. In this case there is a large number (475) of oscillations before the waves separate at $T_s = 86.022 \times 10^5$. The oscillations appear almost periodic for some time $T_0 \leqslant T \leqslant 15.5 \times 10^5$ after the initial transient shedding that occurs for $O \leqslant T < T_0$, where $T_0 = 1.56 \times 10^4$. In this time the energy in E_c plotted in figure 17(*c*) decreases by only 0.2 %, showing that little energy is shed downstream. Subsequently, E_c decreases more rapidly as more energy is shed into the dispersive tails, and the oscillation amplitude and period in figure 17(*a*, *b*) increase until wave

separation occurs. As a measure of the accuracy of these results we note that here, as in the case shown in figure 13, the energy E_m decreases by less than 0.01 % over the time interval shown.

This case corresponds to the isolated point in the parameter space shown in figure 16(*b*) midway between the upper and lower boundaries at $h_1\Delta\rho_1 = 0.03$. Similar almost-periodic initial behaviours with many oscillations and large separation times occur for other cases in this middle region. On the other hand, points near the upper and lower boundaries of the oscillatory region correspond to solutions with very few oscillations.

One of the main questions motivating this work regards the existence of periodic solutions to the given equations. The results shown so far indicate that if periodic solutions exist, they exist for parameters near the middle of the region of oscillations. Indeed, for $T_0 \leqslant T \leqslant 10 \times 10^5$, the present solution in figure 17 appears to be practically periodic. In spite of the demonstrated accuracy of the numerical method, one may question whether numerical errors are not sufficient to depart from any periodic solution, even if it were to exist. The goal of the next section is to describe the solution along vertical crossections of the region of oscillation shown in figure 16, and convincingly demonstrate that, indeed, no periodic solutions are obtained for any of the parameter values.

5.3.3. *Dependence of solution on parameters*

This section describes the dependence of leapfrog solutions on the input parameters by focusing on certain properties of the solution. Figure 18 displays these properties for a range of layer densities $\rho_{1,2,3}$ within the region of oscillation in figure 16, for the case $h_2 = 1$ only. In particular, we let $\rho_2 = 1.05, 1.08, 1.11$ and vary ρ_3, thus sampling a vertical section of the oscillating region. As mentioned earlier, periodic solutions, if they exist, are expected to occur near the centres of these vertical sections.

All results are shown relative to their values at time $T_0 = 500/\tau$, which is chosen to be just past the initial transient. That is, the results are meant to capture changes in the slowly varying regime. Figure 18(*a*) shows the separation time $T_s - T_0$. Three curves are shown, each for a different value of ρ_2, as indicated, and plotted against $\Delta\rho_2$. Each curve is a line connecting the data points for various values of ρ_3, giving rise to various values of $\Delta\rho_2$, within the region of oscillation. The curve for $\rho_2 = 1.05$ has two unconnected branches since no further data points between the branches could be collected owing to the extremely large separation times. As expected, near the borders of the $\rho_2 = 1.08$ and 1.11 regions, the separation times are small, while near the middle of those regions the separation times are large. The partial results for $\rho_2 = 1.05$ may suggest infinite separation times, that is, periodic solutions, in the unresolved interior region. The results for $\rho_2 = 1.08$ and $\rho_2 = 1.11$, on the other hand, indicate that the leapfrog separation time is finite, precluding periodicity.

Figure 18(*b*) exhibits the total number of oscillations N_{osc} that the solution undergoes from $T = T_0$ to $T = T_s$, for the same parameters as in figure 18(*a*). This figure shows that near the boundary of the region of oscillations, where $T_s - T_0$ is small, N_{osc} is small, and near the centre, where $T_s - T_0$ is large, N_{osc} is large, as expected. These curves appear very well resolved, with fewer irregularities than those in figure 18(*a*). The irregularities in figure 18(*a*), particularly for the case $\rho_2 = 1.11$, persist under mesh refinement, and thus do not appear to be caused by lack of resolution. The well-resolved results in figure 18(*b*) for the cases $\rho_2 = 1.08$ and 1.11, again indicate a finite number of leapfrog oscillations, and thus absence of periodicity.

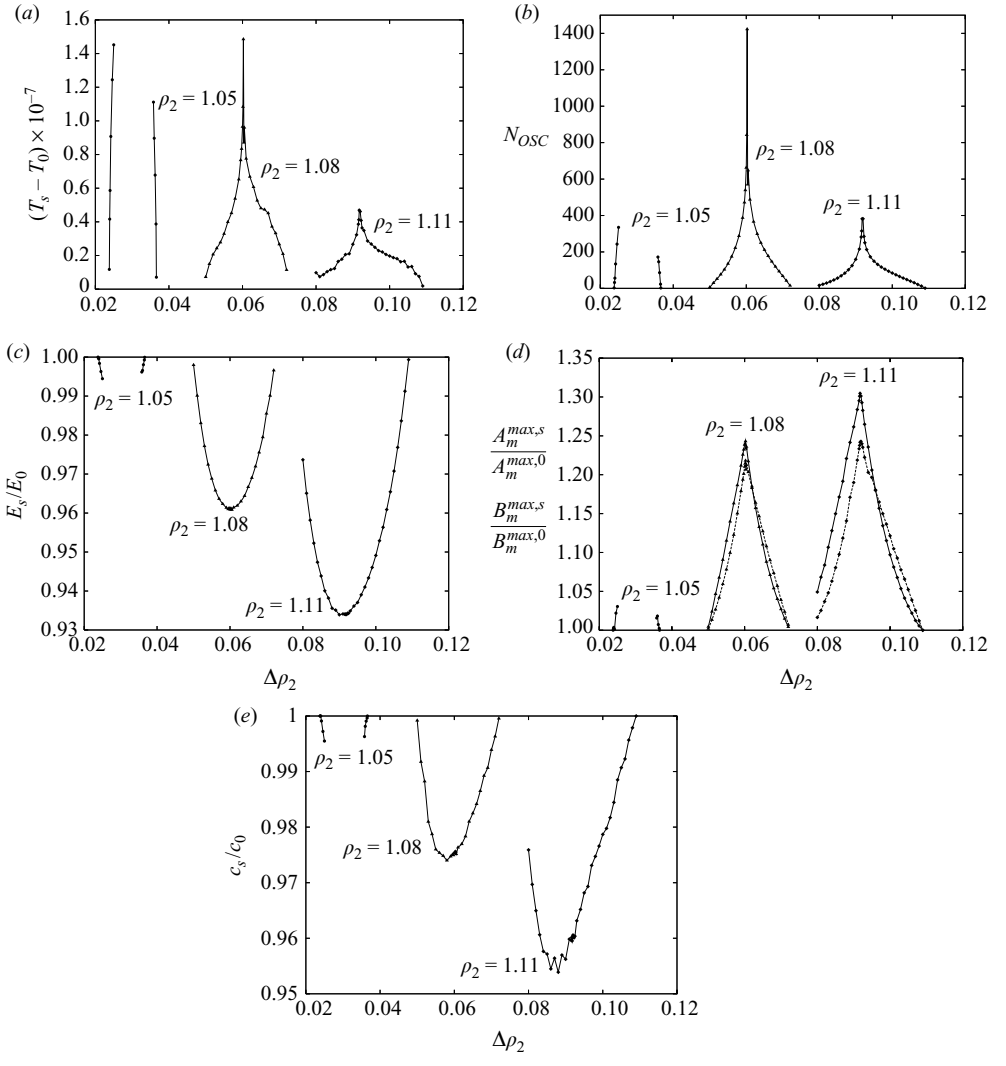

FIGURE 18. Characteristics of the oscillating solutions for the case $h_2 = 1$ and $\rho_2 = 1.05$, 1.08, 1.11, as indicated, versus $\Delta\rho_2$, relative to their values at the time $T_0 = 500/\tau$ chosen to be just past the initial transient. (*a*) Separation time $T_s - T_0$. (*b*) Total number of oscillations N_{osc}. (*c*) Final energy E_s/E_0. (*d*) Maximal amplitude of $A_m(T)$ near T_s, $A_m^{max,s}/A_m^{max,0}$ (solid); same quantity for B (dashed). (*e*) Average translation speed c_s/c_0.

Figure 18(*c–e*) make the case against periodic solutions the strongest. Figure 18(*c*) gives the normalized energy at separation $E_c(T_s)/E_c(T_0)$. These curves, with parabolic shape, are also quite well resolved for $\rho_2 = 1.08$ and 1.11. They show that near the boundary of the region of oscillation, where the separation times are small, the energy decreases only slightly, as expected. However, they also convincingly show that near the middle of the region the energy decreases by a finite, non-zero, amount given by the vertex of the parabola. This fact makes the existence of periodic solutions impossible, since for such solutions the energy would have to be conserved. The fact that the curve is so well-resolved and the method conserves energy (in all cases) to within 0.01 %, eliminates the possibility that the energy loss near the middle regions is a numerical artifact.

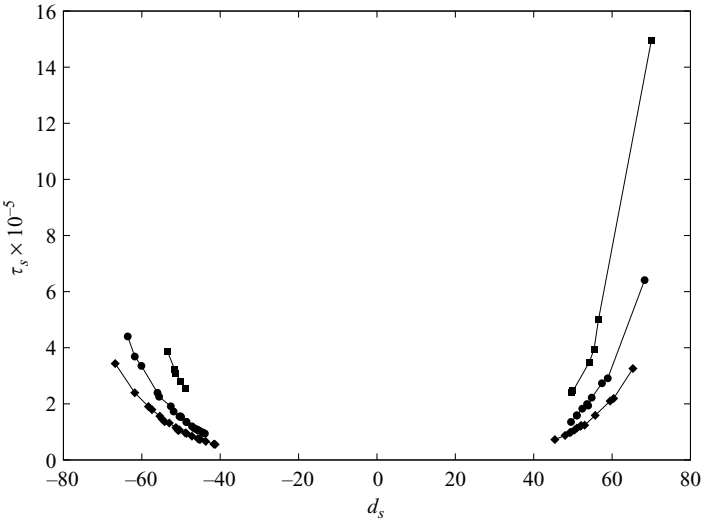

FIGURE 19. Final separation period versus final separation distance for all computed oscillating solutions with $h_2 = 1$, and $\rho_2 = 1.05$ (—■—), 1.08 (—●—), 1.11 (—◆—).

A similar argument can be made with figure 18(*d*,*e*). Figure 18(*d*) shows the maximum amplitude $A_m^{max,s}$, $B_m^{max,s}$ in the oscillation of $A_m(T)$ (solid) and $B_m(T)$ (dashed) near T_s normalized by the respective maximum amplitudes near T_0, $A_m^{max,0}$, $B_m^{max,0}$. Figure 18(*e*) presents the average translation speed c_s of the two waves at T_s normalized by the average translation speed at T_0. Figure 18(*d*, *e*) show that near the boundary of the oscillating region, the maximum amplitude and the translation speed at separation remain close to their initial values. Near the interior of the region, however, the maximum amplitudes at separation are distinctly larger than the initial amplitudes, and the translation speeds at separation are distinctly smaller than the intial speeds. The irregularities in figure 18(*e*) near the minima for $\rho_2 = 1.08$ and 1.11 may be caused by difficulties in accurately determining the average translations speeds. Nonetheless, figure 18(*d*, *e*) convincingly show that periodic solutions, for which the maximum amplitude and translation speed would have to remain constant, do not occur.

Figure 19 shows how the oscillation period τ_s just before separation varies with the final maximal signed separation distance $d_s = \xi_A - \xi_B$ for all oscillating solutions obtained with $h_2 = 1$. The data corresponding to equal values of ρ_2 are connected by solid curves. Note that the data follows well defined trends, indicating that a relation between τ_s and d_s holds in all cases. Note also that the largest separation distances observed are $\leqslant 70$ in magnitude. We take this as an asymptotic limit on the value of d_s for which leapfrog behaviour can be observed for the range of parameters in this study.

6. Asymptotic model

We now turn to the description of a simple asymptotic model which can be used to interpret our numerical results. This model is similar to that developed by Liu *et al.* (1982) for the same purpose, but as described below, we need to extend the LPK model to allow for finite spatial separations between the solitary waves on each pycnocline, and to incorporate the effect of the trailing radiation.

Our starting point is the basic coupled evolution equations (3.1). These equations possess the exact energy relations

$$\frac{\mathrm{d}}{\mathrm{d}T}\int_{-\infty}^{\infty}\frac{A^2}{2\beta_1}\mathrm{d}\xi = -\frac{\mathrm{d}}{\mathrm{d}T}\int_{-\infty}^{\infty}\frac{B^2}{2\beta_2}\mathrm{d}\xi = m_1 m_2\int_{-\infty}^{\infty}A\mathscr{H}(B)\mathrm{d}\xi = m_1 m_2\int_{-\infty}^{\infty}B\mathscr{H}(A)\mathrm{d}\xi. \tag{6.1}$$

Elimination of the coupling term yields

$$\int_{-\infty}^{\infty}\frac{A^2}{2\beta_1}\mathrm{d}\xi + \int_{-\infty}^{\infty}\frac{B^2}{2\beta_2}\mathrm{d}\xi = \text{constant} \tag{6.2}$$

expressing the conservation of total energy, as discussed in § 5.1.2; (see (5.3)). Equation (6.1) describes the exchange of energy between the A, B waves in explicit form. Then, as in Liu *et al.* (1982), we suppose that the coupling between the waves is weak (i.e. formally $H_2 \to \infty$), so that at the leading order we solve each equation when the coupling term is omitted. In this limit, the uncoupled solitary wave solutions can be found for the uncoupled equations, which then reduce to an intermediate long wave equation (see Ablowitz and Segur 1981) with Joseph (1977) solitary waves as solutions. For simplicity we also suppose that $H_1 = H_2 = H_3$, which is the only case considered numerically in this paper. Thus we suppose that each uncoupled equation has an asymptotic solution which at leading order is just a Joseph soliton given by (cf. (3.8)),

$$A(\xi, T) \sim \frac{H(1+\cos\delta_1)}{\cos\delta_1 + \cosh\frac{\delta_1 X}{H_1}} \quad \text{where} \quad X = \xi - \Phi, \quad \Phi = \int_{T_1}^{T} V(T')\mathrm{d}T', \tag{6.3a}$$

$$B(\xi, T) \sim \frac{K(1+\cos\delta_2)}{\cos\delta_2 + \cosh\frac{\delta_2 Y}{H_3}} \quad \text{where} \quad Y = \xi - \Psi, \quad \Psi = \int_{T_2}^{T} W(T')\mathrm{d}T', \tag{6.3b}$$

where

$$\frac{\mathrm{d}\Phi}{\mathrm{d}T} = V, \quad V + \Delta = -\frac{\beta_1}{H_1}\left(\frac{\rho_1}{\rho_2} + m_1^2\right)\delta_1\cot\delta_1, \quad \delta_1\tan\frac{\delta_1}{2} = \frac{H\,H_1\alpha_1}{2\beta_1\left(\dfrac{\rho_1}{\rho_2} + m_1^2\right)}, \tag{6.4a}$$

$$\frac{\mathrm{d}\Psi}{\mathrm{d}T} = W, \quad W - \Delta = -\frac{\beta_2}{H_3}\left(\frac{\rho_3}{\rho_2} + m_2^2\right)\delta_2\cot\delta_2, \quad \delta_2\tan\frac{\delta_2}{2} = \frac{K\,H_3\alpha_2}{2\beta_2\left(\dfrac{\rho_3}{\rho_2} + m_2^2\right)}. \tag{6.4b}$$

Here we have assumed that the effect of the coupling is to cause the amplitudes (H, K) and hence the velocities (V, W) to vary slowly with time T. The constants $T_{1,2}$ determine the initial positions of the solitary waves. A formal asymptotic expansion will then yield the desired equations for H and K (or V and W). But we can proceed more simply by using the energy equations (6.1) evaluated at the leading order with (6.3*a*,*b*). The result is a set of two equations for H, K, Φ, Ψ which are then combined with the expressions (6.4*a*,*b*) to form four first order in time ordinary differential equations for the four unknowns. The system can be reduced to three since in the first two equations, only the relative position $P = \Phi - \Psi$ appears, where

$$\frac{\mathrm{d}P}{\mathrm{d}T} = V - W = -2\Delta - \frac{\beta_1}{H_1}\left(\frac{\rho_1}{\rho_2} + m_1^2\right)\delta_1\cot\delta_1 + \frac{\beta_2}{H_3}\left(\frac{\rho_3}{\rho_2} + m_2^2\right)\delta_2\cot\delta_2\,. \tag{6.5}$$

There is a further reduction to two equations as the total energy is conserved (6.2), and these can then be analysed using phase-plane methods. Note that the relative position equals the separation distance between the waves as defined in (5.2).

The next step is to evaluate the energy integrals in (6.1) using the expressions (6.3*a*,*b*) to get

$$E_1(\delta_1) = \int_{-\infty}^{\infty} \frac{A^2}{2\beta_1} \mathrm{d}\xi = \frac{4\beta_1 \left(\dfrac{\rho_1}{\rho_2} + m_1^2\right)^2}{H_1 \alpha_1^2} \delta_1 (1 - \delta_1 \cot \delta_1), \tag{6.6a}$$

$$E_2(\delta_2) = \int_{-\infty}^{\infty} \frac{B^2}{2\beta_2} \mathrm{d}\xi = \frac{4\beta_2 \left(\dfrac{\rho_3}{\rho_2} + m_2^2\right)^2}{H_3 \alpha_2^2} \delta_2 (1 - \delta_2 \cot \delta_2). \tag{6.6b}$$

The coupling integral I in (6.1) is evaluated using Parseval's theorem so that

$$\frac{I}{m_1 m_2} = \int_{-\infty}^{\infty} A \mathscr{H}(B) \mathrm{d}\xi = \frac{1}{2\pi} \int_{-\infty}^{\infty} \widehat{A}(-k) \widehat{\mathscr{H}(B)}(k) \mathrm{d}k, \tag{6.7}$$

where the Fourier transforms of A, B are given by

$$\widehat{A}(k) = \frac{4\beta_1 \left(\dfrac{\rho_1}{\rho_2} + m_1^2\right)}{\alpha_1} \frac{\pi \sinh(kH_1)}{\sinh(\pi k H_1/\delta_1)} \exp(-\mathrm{i}k\Phi), \tag{6.8a}$$

$$\widehat{B}(k) = \frac{4\beta_2 \left(\dfrac{\rho_3}{\rho_2} + m_2^2\right)}{\alpha_2} \frac{\pi \sinh(kH_3)}{\sinh(\pi k H_3/\delta_3)} \exp(-\mathrm{i}k\Psi). \tag{6.8b}$$

Then, it follows that

$$I = \frac{16\pi^2 m_1 m_2 \beta_1 \beta_2 \left(\dfrac{\rho_1}{\rho_2} + m_1^2\right)\left(\dfrac{\rho_3}{\rho_2} + m_2^2\right)}{\alpha_1 \alpha_2} \tilde{I}(\delta_1, \delta_2, P), \tag{6.9a}$$

$$\tilde{I}(\delta_1, \delta_2, P) = \frac{1}{2\pi} \int_{-\infty}^{\infty} \frac{-\mathrm{i}k^2 \sinh kH_2}{\sinh(\pi k H_2/\delta_1) \sinh(\pi k H_2/\delta_2)} \exp(\mathrm{i}kP) \mathrm{d}k. \tag{6.9b}$$

Note that we have simplified this expression for $\tilde{I}$ using our assumption that $H_1 = H_3 = H_2$. When the energy expressions (6.6*a*,*b*) and (6.9*a*) are substituted into (6.1) and combined with (6.5), we obtain the desired system of ordinary differential equations for δ_1, δ_2, P, which can be analysed by phase-plane methods. This is the same system considered by Liu *et al.* (1982). However, it is still too complicated to obtain simple explicit solutions, so we will follow Liu *et al.* and make a further approximation that the solitary waves are close to being BO solitary waves. But, unlike Liu *et al.*, we will crucially not assume that P is small.

The expressions (6.3*a*,*b*) collapse to the BO solitary waves in the limit $H_{1,3} \to \infty$, $\delta_{1,3} \to \pi$, where if we write $\delta_{1,3} = \pi - \sigma_{1,3}$ then $H_{1,3}\sigma_{1,3} = \pi\lambda_{1,3}$ is kept constant. The outcome is

$$A \sim \frac{H\lambda_1^2}{X^2 + \lambda_1^2}, \quad B \sim \frac{K\lambda_3^2}{Y^2 + \lambda_3^2}, \tag{6.10}$$

where $$V + \Delta = \frac{\alpha_1 H}{4} = \frac{\beta_1}{\lambda_1}\left(\frac{\rho_1}{\rho_2} + m_1^2\right), \quad W - \Delta = \frac{\alpha_2 K}{4} = \frac{\beta_2}{\lambda_3}\left(\frac{\rho_3}{\rho_2} + m_2^2\right). \tag{6.11}$$

In this approximation, the energy integrals become

$$E_1 = \frac{M_0 H}{4\beta_1}, \quad E_2 = \frac{N_0 K}{4\beta_2}, \tag{6.12}$$

$$\text{where} \quad M_0 = \pi H \lambda_1 = \frac{4\pi\beta_1}{\alpha_1}\left(\frac{\rho_1}{\rho_2} + m_1^2\right), \quad N_0 = \pi K \lambda_3 = \frac{4\pi\beta_2}{\alpha_2}\left(\frac{\rho_3}{\rho_2} + m_2^2\right). \tag{6.13}$$

Note that M_0, N_0 are the mass of the waves, and in the BO approximation are constants. It follows that evaluation of (6.9*b*) gives

$$\tilde{I} = \frac{\pi^2}{4H_2^3}\tanh\left(\frac{\pi P}{2H_2}\right)\operatorname{sech}^2\left(\frac{\pi P}{2H_2}\right). \tag{6.14}$$

Remarkably, in this approximation, I depends only on P. Hence the energy equations (6.1) become

$$\frac{M_0}{4\beta_1}\frac{\mathrm{d}H}{\mathrm{d}T} = -\frac{N_0}{4\beta_2}\frac{\mathrm{d}K}{\mathrm{d}T} = \left(\frac{\pi^3 m_1 m_2 M_0 N_0}{8H_2^4}\right) F(P), \tag{6.15a}$$

$$F(P) = \frac{2H_2}{\pi}\tanh\left(\frac{\pi P}{2H_2}\right)\operatorname{sech}^2\left(\frac{\pi P}{2H_2}\right). \tag{6.15b}$$

Next we see that in this same limit, the velocity equation (6.5) becomes

$$\frac{\mathrm{d}P}{\mathrm{d}T} = V - W = -2\Delta + \frac{\alpha_1 H}{4} - \frac{\alpha_2 K}{4}. \tag{6.16}$$

This can be now combined with (6.15*a*) to obtain a single second-order ordinary differential equation for P

$$\frac{\mathrm{d}^2 P}{\mathrm{d}T^2} + \Omega^2 F(P) = 0, \tag{6.17a}$$

$$\Omega^2 = -\frac{\pi^4 m_1 m_2 \beta_1 \beta_2}{2H_2^4 \alpha_1 \alpha_2}\left[\alpha_1^2\left(\frac{\rho_3}{\rho_2} + m_2^2\right) + \alpha_2^2\left(\frac{\rho_1}{\rho_2} + m_1^2\right)\right]. \tag{6.17b}$$

Note that in general Ω^2 can be either positive or negative, but it is positive for all the system parameters that we have considered, since here $\beta_{1,2} > 0$, $\alpha_{1,2} > 0$, $m_1 m_2 < 0$. In the limit $P \to 0$ and $F(P) \to P$, (6.17*a*) collapses to the simple harmonic oscillator equation obtained by Liu *et al.* (1982). However, as we now discuss below, it is crucial that we have retained finite values of P.

We examine the solutions of (6.17*a*) in the P–Q phase plane where $Q = \mathrm{d}P/\mathrm{d}T$. Since $F(P) \neq 0$ for all finite non-zero P, there is a single critical point at $P = Q = 0$. The linearized system about this equilibrium is $\mathrm{d}^2P/\mathrm{d}T^2 + \Omega^2 P = 0$, and thus the equilibrium is a centre point for $\Omega^2 > 0$ and a saddle point for $\Omega^2 < 0$. Therefore, the linear result is that, when $\Omega^2 > 0$, leapfrogging occurs with an oscillation frequency of Ω, and when $\Omega^2 < 0$ there is immediate separation. This is the same result obtained by Liu *et al.* (1982).

However, *all* our numerical results are for the case when $\Omega^2 > 0$, and we found many cases when there was immediate separation. Hence it is necessary to examine the nonlinear phase plane more closely. Equation (6.17*a*) can be integrated once to give

$$\left(\frac{\mathrm{d}P}{\mathrm{d}T}\right)^2 + \Omega^2 G(P) = E_0, \tag{6.18a}$$

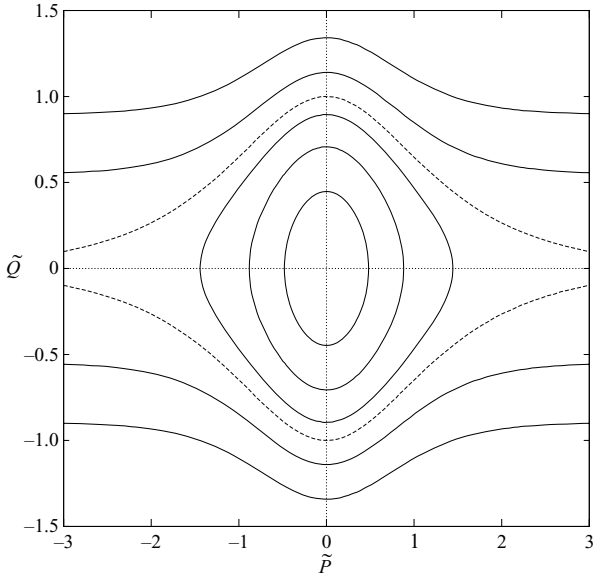

FIGURE 20. Phase plane for (6.18*a*) with $\Omega^2 > 0$, where $\widetilde{P} = \pi P/2H_2$ and $\widetilde{Q} = \pi Q/(2H_2\Omega)$. The separatrix is shown by the dashed curves.

$$G(P) = \frac{4H_2^2}{\pi^2}\tanh^2\left(\frac{\pi P}{2H_2}\right), \tag{6.18b}$$

where E_0 is a constant of integration determined by the initial conditions. Equation (6.18) describes the solution curves in the P–Q phase plane. These are plotted in figures 20 and 21, where we replace P with $\widetilde{P} = \pi P/2H_2$ and absorb Ω into the time scale, $\widetilde{T} = \Omega T$, so that $\widetilde{Q} = \mathrm{d}\widetilde{P}/\mathrm{d}\widetilde{T} = \pi Q/(2H_2\Omega)$.

Figure 20 shows the case when $\Omega^2 > 0$, as in our simulations. As expected from the linearization, initial conditions close to the origin yield periodic solutions, that is, leapfogging occurs. But for initial conditions sufficiently far from the origin, the waves immediately separate, with the separation distance P increasing monotonically. The boundary between these regimes is given by a separatrix, shown as a dashed line. Near the origin, the orbits are approximately circles, describing sinusoidal oscillations with period $2\pi/\Omega$. But as the amplitude increases, so does the oscillation period, which becomes infinite on the separatrix.

The separatrix is the orbit for which $Q \to 0$ as $P \to \pm\infty$, given by

$$Q^2 = \frac{4H_2^2\Omega^2}{\pi^2}\mathrm{sech}^2\left(\frac{\pi P}{2H_2}\right). \tag{6.19}$$

Initial conditions outside this separatrix that give immediate separation are defined by the constraint

$$Q_0^2 > \frac{4H_2^2\Omega^2}{\pi^2}\mathrm{sech}^2\left(\frac{\pi P_0}{2H_2}\right). \tag{6.20}$$

Here the subscript 0 denotes the initial values. It follows that any initial value Q_0 will terminate the leapfrog activity if the initial wave separation distance P_0 is sufficiently large. Also, if $Q_0^2 > 4H_2^2\Omega^2/\pi^2$ then there is separation for *any* value of P_0. Using

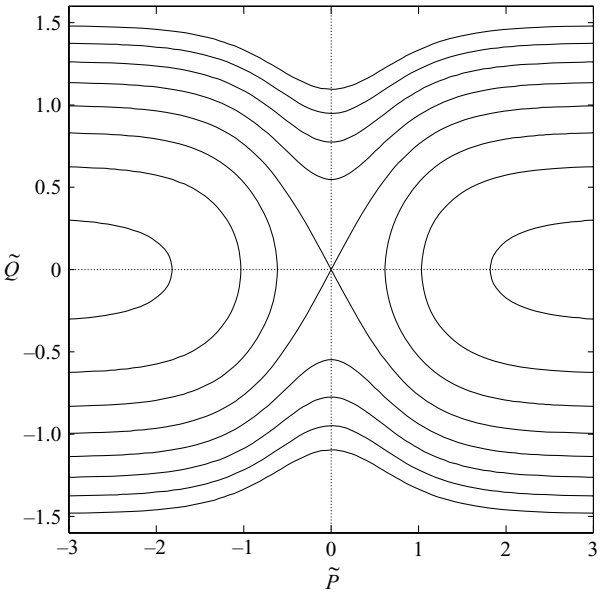

FIGURE 21. Phase plane for (6.18*a*) with $\Omega^2 < 0$, where P, Q are normalized as in figure 21.

(6.16) we find that Q_0 is related to the initial amplitudes by the equation

$$Q_0 = \left.\frac{\mathrm{d}P}{\mathrm{d}T}\right|_{T=0} = -2\Delta + \frac{1}{4}(\alpha_U H_0 - \alpha_L K_0). \tag{6.21}$$

It follows that $|Q_0|$ increases with $|\Delta|$, and it also increases with the difference in the initial amplitudes, which might be expected. In the case $\Omega^2 > 0$, figure 20 shows that all orbits which pass to infinity do so with a decrease in $|Q|$. In view of (6.16), this means there is a decrease in the difference between the amplitudes from the initial state to the final state.

It is also useful to plot the phase plane for the case $\Omega^2 < 0$, in normalized $\widetilde{P}$–$\widetilde{Q}$ coordinates, as shown in figure 21. As expected, the origin is a saddle point, and all orbits pass to infinity, that is, no leapfrogging occurs. Note that now on all orbits the final value of $|Q|$ is larger than the initial value. Because in this case $\alpha_{1,2}$ have opposite signs, this means that one amplitude must increase from its initial value and the other then decreases.

In order to compare our asymptotic model to our numerical results, figure 22 plots the computed values of $\widetilde{P}$ and $\widetilde{Q}$ for different trajectories. The actual system is supposed to be a perturbation of the model. Indeed, the leapfrogging solution (LF) starts within an apparent separatrix, which is in fact an unstable spiral, that oscillates until the final separation occurs. The two cases of immediate separation ($S1$ and $S2$) begin outside the apparent separatrix. Other cases (not shown here) have qualitatively similar behaviours. Note, first, that the exact position of the apparent separatrix is not identical to the one in the model shown in figure 20. This is evident by comparing the dashed curve in figure 22, which is the model's separatrix, with the apparent numerical separatrix. Thus, the model qualitatively predicts the behaviour observed numerically. Quantitatively, the position of the model's separatrix differs from the numerical approximate separatrix by about 25 % at $\widetilde{P} = 0$. At larger values of $|\widetilde{P}|$ the two compare much more favourably. Note, secondly, that the initial conditions for

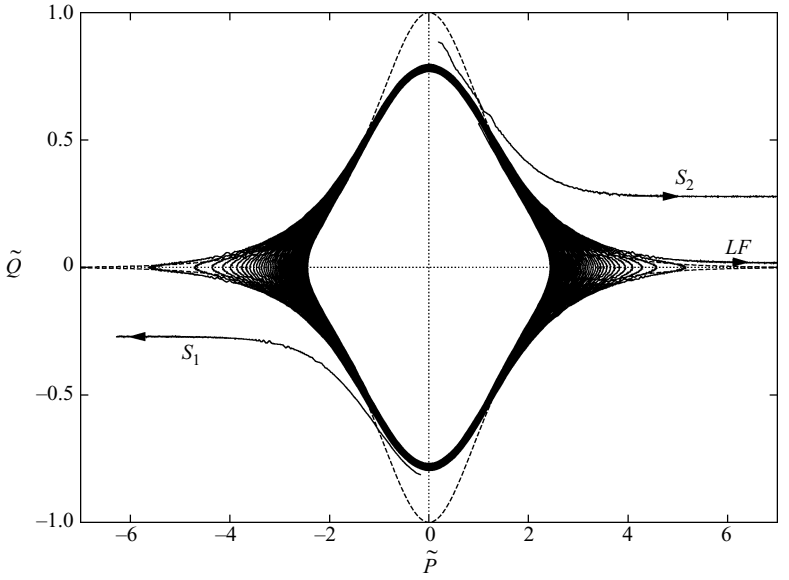

FIGURE 22. Phase plane for the numerical results; the orbit LF is a leapfrogging case, and the orbits $S1$, $S2$ are those with immediate separation. The dashed curve is the separatrix for the model, equal to the dashed curve in figure 20.

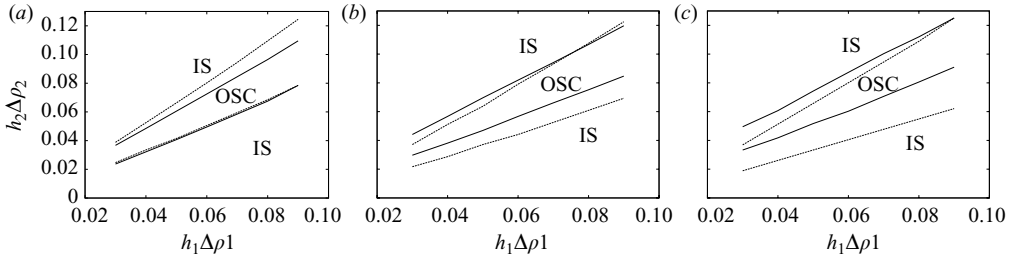

FIGURE 23. Regions in the parameter space $h_1\Delta\rho_1$–$h_2\Delta\rho_2$ for which the chosen initial conditions lead to oscillations, as computed numerically (region between solid lines) and as follows from the asymptotic results (region between dashed lines). In all cases, $h_1 = 1$, $\rho_1 = 1.02$. (*a*) $h_2 = 1.0$, (*b*) $h_2 = 1.4$, (*c*) $h_2 = 1.8$. The labels IS and OSC denote immediate separation and oscillations, respectively.

the shown leapfrogging solution start very close to the approximate separatrix, and thus one cannot expect the oscillation frequency to be close to the linearly predicted frequency of Ω. This is consistent with our observations in § 5.1.3 and is true for all our numerical solutions where parameters were chosen to obtain wave separation in a computable time. This automatically places our solution far from the origin and close to the approximate separatrix.

Another quantitative comparison between the asymptotic model and the numerical results is shown in figure 23. This figure shows the regions in the parameter space $h_1\Delta\rho_1$–$h_2\Delta\rho_2$ corresponding to oscillating solutions (OSC) and to immediately separating solutions (IS), using different values of $h_2 = 1, 1.4, 1.8$. The regions computed numerically are the ones bounded by the solid lines, and agree with those shown in figure 16(*a–c*). The regions obtained from asymptotic model are the ones

bounded by the dashed lines. They are obtained using condition (6.20) and equation (6.21) with $P_0 = 0$, $H_0 = K_0 = 0.5$. As before, the values of $\alpha_1, \alpha_2, c_1, c_2$ corresponding to given values of $\rho_{1,2,3}, h_{1,2}$ are obtained from solutions to the eigenvalue problem (3.4). The figure shows that the region of oscillation obtained from the asymptotic model roughly predicts the region obtained numerically.

Note that the model is developed for Joseph solitary waves, as in Liu *et al.* (1982), but in order to get some simple expressions it is reduced to BO waves, again as in Liu *et al.* For the parameters we use, we did check this approximation and doubt that it significantly affects the comparison between the asymptotic theory and the numerical results presented in figure 23.

Finally, we turn to an estimate of the effect of the trailing radiation seen in the numerical solutions. Although this could be attempted by extending the asymptotic analysis it seems quite difficult and would mean carrying the asymptotic model through to a higher order. Instead we present a qualitative argument. We return to (6.1) and replace them with

$$\frac{\mathrm{d}}{\mathrm{d}T}\int_{-\infty}^{\infty}\frac{A^2}{2\beta_1}\mathrm{d}\xi = m_1 m_2\int_{-\infty}^{\infty}A\mathscr{H}(B)\mathrm{d}\xi - \epsilon_1, \tag{6.22a}$$

$$\frac{\mathrm{d}}{\mathrm{d}T}\int_{-\infty}^{\infty}\frac{B^2}{2\beta_2}\mathrm{d}\xi = m_1 m_2\int_{-\infty}^{\infty}B\mathscr{H}(A)\mathrm{d}\xi - \epsilon_2. \tag{6.22b}$$

Here $\epsilon_{1,2} > 0$ represent the rate of energy loss from each solitary wave component due to the generation of each radiating tail. This will depend on A, B in some way to be estimated. It now follows that (6.15*a*) is replaced by

$$\frac{M_0}{4\beta_1}\frac{\mathrm{d}H}{\mathrm{d}T} + \epsilon_1 = -\frac{M_0}{4\beta_1}\frac{\mathrm{d}H}{\mathrm{d}T} - \epsilon_2 = \left(\frac{\pi^3 m_1 m_2 M_0 N_0}{8H_2^4}\right)F(P), \tag{6.23}$$

and ultimately (6.17*a*) is replaced by

$$\frac{\mathrm{d}^2 P}{\mathrm{d}T^2} + \Omega^2 F(P) = \epsilon \equiv -\frac{\alpha_1\beta_1\epsilon_1}{M_0} + \frac{\alpha_2\beta_2\epsilon_2}{N_0}. \tag{6.24}$$

We must now estimate the sign of ϵ. Because, owing to the moving frame of reference, the radiating tail propagates to the left, we infer that the component which is also at some instant propagating to the left will be more effective in emitting radiation. Thus when $V > W$, $\mathrm{d}P/\mathrm{d}T > 0$, the B wave is emitting radiation, and so ϵ_2 is largest when $\mathrm{d}P/\mathrm{d}T > 0$; on the other hand, ϵ_1 is largest when $\mathrm{d}P/\mathrm{d}T < 0$. It follows that ϵ will have the same sign as $\mathrm{d}P/\mathrm{d}T$, which is then easily seen to be destabilizing. In other words, due to the radiation, the origin of the P–Q phase plane will become an unstable spiral point instead of a centre point. Physically this is interpreted as saying that when $V > W$, the B wave emits more radiation than the A wave, and so its amplitude decreases and the difference $V - W$ gets larger, enhancing the separation between the components. The reverse happens when $V < W$ as then it is the A wave which emits more radiation, decreasing its amplitude now making the difference $W - V$ larger, which again enhances the separation between the components.

7. Summary

A highly accurate numerical method was used to resolve the evolution of two localized disturbances on neighbouring pycnoclines. Earlier experimental and numerical work by Weidman & Johnson (1982) and Liu *et al.* (1982) indicated

the existence of nearly periodic oscillatory solutions, in which the solitary-wave-like disturbance on each pycnocline oscillates about the position of the analogous disturbance on the other pycnocline, leading to the notion of leapfrogging. In this paper, these oscillating solutions were computed over large times for a range of parameters. The numerical method accurately conserves energy and the results have converged to several digits under mesh refinement. Two distinct regimes are identified. In the first, the initial localized disturbances immediately separate, and two pure solitary waves of the full system form, with different speeds, each characterized by a main disturbance in one pycnocline, and a small accompanying disturbance in the other pycnocline. The second regime is that where at first the disturbances exhibit leapfrogging behaviour, but due to the small emission of radiation during the oscillations, the disturbances eventually separate and again the outcome is two pure solitary wave solutions. We exhibit the region in parameter space where this leapfrogging regime holds, and describe the characteristics of the solutions as a function of the input parameters. Conclusive evidence is given showing that no permanent periodic solutions appear for any values in the parameter space, owing to the radiated energy lost from the primary waves to their dispersive tails. As a result, the spatial oscillations grow slowly in amplitude and period until ultimately the solitary waves can no longer communicate with one another at which point they separate out as pure solitary waves each with their own speed. These results are similar to those of Wright & Scheel (2007). However, in their case the coupling occurs only through nonlinear terms, and in ours it is only through linear dispersion terms. Note that the numerical results strongly indicate that the oscillations are coupled to energy radiation and thus purely periodic oscillations cannot exist for any initial conditions, not just the ones we have chosen. Nevertheless, conclusive evidence to this effect requires further theoretical study. We also extended the asymptotic model of Liu *et al.* in which the leapfrogging behaviour is modelled as a weak-interaction between two BO type solitary waves belonging to each pycnocline. This theoretical model leads to a simple ordinary differential equation system which can be explicitly solved, and whose solutions provide a very good qualitative description of both regimes, with reasonable quantitative agreement.

M. Nitsche gratefully acknowledges the support of the National Science Foundation through the grant DMS-0308061 and B. Fornberg through the grants DMS-0611681 and ATM-0620068. M. Ghrist is supported by NASA grant NPSCOCG1035B and NSF grant DMS-9256335. We also thank the reviewers, in particular for the suggestion that led to figure 23.

Appendix. Derivation of evolution equations

In this appendix we derive, in a systematic manner, the two-pycnocline evolution equations. For the linear terms in these equations, it is sufficient to consider only the linearized equations. Addition of the nonlinear terms to each evolution equation then closes the system.

We consider the same three-layer configuration as in Liu *et al.* (1980) (see figure 3). The layer depths H_1, H_2, H_3 form regions I, II, III, each with constant density, but separated by two pycnoclines of thickness $2h_1$, $2h_2$, within which the density $\overline{\rho}(z)$ varies continuously from one constant value to another. In our notation z is the upward coordinate and the fluid is contained between rigid horizontal boundaries at $z = 0, H$.

For two-dimensional flow, the streamfunction satisfies the equation

$$[(\overline{\rho}\psi_z)_z + \overline{\rho}\psi_{xx}]_{tt} + \overline{\rho}N^2\psi_{xx} = 0, \tag{A 1}$$

where $N^2 = -g\overline{\rho}_z/\overline{\rho}$ is the square of the continuously varying Brunt–Väsälä frequency. The fact that the upper and lower boundaries are impermeable require that $\psi = 0$ at $z = 0, H$. In the sequel we adopt the shorthand notation $z^{\pm}_{1,2}$ for the top and bottom edges of the upper (U) and lower (L) pycnoclines respectively,

$$\left.\begin{aligned} z_1^+ &= H_2 + H_3 + 2h_1 + 2h_2, \quad z_1^- = H_2 + H_3 + 2h_2, \\ z_2^+ &= H_3 + 2h_2, \quad z_2^- = H_3\,. \end{aligned}\right\} \tag{A 2}$$

For this linearized problem, it is convenient to work in Fourier space. Thus we seek a solution of (A 1) in the form $\psi(x, z, t) = \phi(z)\exp(\mathrm{i}kx - \mathrm{i}\omega t)$, so that

$$(\overline{\rho}\phi_z)_z - k^2\overline{\rho}\phi + \frac{\overline{\rho}N^2}{c^2}\phi = 0, \tag{A 3}$$

where $c = \omega/k$. This equation holds throughout. But in regions I, II, III the density is constant, and hence the respective solutions of (A 3) with $N^2 = 0$ are

$$\left.\begin{aligned} \phi &= A\frac{\sinh k(H - z)}{\sinh kH_1}, \quad \text{in I,} \\ \phi &= A'\,\frac{\sinh k(z - z_2^+)}{\sinh kH_2} + B'\,\frac{\sinh k(z_1^- - z)}{\sinh kH_2}, \quad \text{in II,} \\ \phi &= -B\frac{\sinh kz}{\sinh kH_3}, \quad \text{in III.} \end{aligned}\right\} \tag{A 4}$$

In the upper and lower pycnoclines we have

$$\phi = A\phi_1(z) \quad \text{in U}, \quad \phi = B\phi_2(z) \quad \text{in L}, \tag{A 5}$$

where each of $\phi_{1,2}$ satisfy the full equation (A 3) in U, L respectively. The modal functions are normalized to unity according to

$$\phi_1(z_1^+) = 1, \quad \phi_2(z_2^-) = -1. \tag{A 6}$$

Thus $A, -B$ are the values of ϕ at the upper and lower boundaries of U, L respectively.

The solutions are now completed by requiring that ϕ, ϕ_z are continuous at the boundaries between U, L and the regions I, II, III. Continuity of ϕ at the top and bottom boundaries has already been satisfied by the normalization conditions (A 6), while continuity of ϕ_z at these boundaries gives the conditions

$$-\frac{k}{\tanh kH_1} = \phi_{1z}(z_1^+), \quad -\frac{k}{\tanh kH_3} = \phi_{2z}(z_2^-). \tag{A 7}$$

Now we see that (A 6) and (A 7) specify each of $\phi_{1,2}$ uniquely as functions of z, k, c. Next, continuity of the modal functions and their derivatives applied at the lower, upper boundaries of U, L respectively give

$$\left.\begin{aligned} &Am_1 = A', \quad Bm_2 = B', \quad An_1 = A'\,\frac{k}{\tanh kH_2} - B'\,\frac{k}{\sinh kH_2}, \\ &Bn_2 = A'\,\frac{k}{\sinh kH_2} - B'\,\frac{k}{\tanh kH_2}, \end{aligned}\right\} \tag{A 8}$$

where we have introduced the shorthand notation

$$m_1 = \phi_1(z_1^-), \quad m_2 = \phi_2(z_2^+), \quad n_1 = \phi_{1z}(z_1^-), \quad n_2 = \phi_{2z}(z_2^+). \tag{A 9}$$

Note that the constants $m_{1,2}$ and $n_{1,2}$ are uniquely determined as functions of k, c.

Finally elimination of A', B' yields the two-by-two system for the amplitudes A, B

$$D_1(\omega, k)A + E_1(\omega, k)B = 0, \quad E_2(\omega, k)A + D_2(\omega, k)B = 0. \tag{A 10}$$

Here D_1, D_2 can be interpreted as respectively the dispersion relations for the upper, lower pycnoclines, while E_1, E_2 are the coupling terms; they are given by

$$\left.\begin{aligned} D_1(\omega, k) &= \frac{m_1 k}{\tanh kH_2} - n_1, \quad D_2(\omega, k) = \frac{m_2 k}{\tanh kH_2} + n_2, \\ E_1(\omega, k) &= -\frac{m_2 k}{\sinh kH_2}, \quad E_2(\omega, k) = -\frac{m_1 k}{\sinh kH_2}. \end{aligned}\right\} \tag{A 11}$$

The determinant of the two-by-two system (A 10) then yields the dispersion relation for the full system.

We are, however, concerned with the limit $k \to 0$ when there is a near resonance between waves on U, L. Hence we introduce a small parameter ϵ such that $k \sim \epsilon$, but H_1, H_2, H_3 are all $O(1/\epsilon)$. Then we seek an expansion in ϵ, in which it will be sufficient to keep only the leading $O(\epsilon)$ terms. It follows that the k^2 term in (A 3) can be omitted and each of ϕ_1, ϕ_2 satisfy the long-wave modal equation,

$$(\overline{\rho}\phi_z)_z + \frac{\overline{\rho}N^2}{c^2}\phi = 0. \tag{A 12}$$

Next we write

$$\phi_{1,2} = \phi_{1,2}^{(0)} + \phi_{1,2}^{(1)} + \cdots, \quad c = c^{(0)} + c^{(1)} + \cdots. \tag{A 13}$$

At leading order, $\phi_{1,2}^{(0)}$ satisfy (A 12) with $c = c^{(0)}$ and the boundary conditions obtained from (A 7) and (A 8),

$$\phi_{1z}^{(0)}(z_1^-) = \phi_{1z}^{(0)}(z_1^+) = 0, \quad \phi_{2z}^{(0)}(z_2^-) = \phi_{2z}^{(0)}(z_2^+) = 0. \tag{A 14}$$

Note here that the expressions (A 9) imply that n_1, n_2 are $O(\epsilon)$. Thus at this leading order the modes $\phi_{1,2}^{(0)}$ uncouple, and the eigenvalue $1/c^2$ in (A 12) is determined separately for each mode. Consequently, we have two independent modes denoted as $c^{(0)} = c_{1,2}^{(0)}$, respectively.

Next, for resonant coupling we must have $c_1^{(0)} = c_2^{(0)} = c_0$. It is convenient to allow for an $O(\epsilon)$ detuning so that we write

$$c_{1,2}^{(0)} = c_0 \pm \Delta \tag{A 15}$$

where Δ is $O(\epsilon)$. Of course strictly the detuning term should appear in conjunction with $c^{(1)}$ as follows. The equations describing the first corrections to $\phi_{1,2}^{(0)}$ are given by

$$\left(\overline{\rho}\left(\phi_{1,2}^{(1)}\right)_z\right)_z + \frac{\overline{\rho}N^2}{c_0^2}\phi_{1,2}^{(1)} = \frac{2\overline{\rho}N^2\left(c^{(1)} \pm \Delta\right)}{c_0^3}\phi_{1,2}^{(0)}, \tag{A 16}$$

which satisfy the upper and lower pycnocline boundary conditions

$$\left.\begin{aligned} \phi_1^{(1)}(z_1^+) = 0, \quad \phi_{1z}^{(1)}(z_1^+) &= -\frac{k}{\tanh kH_1}, \\ \phi_2^{(1)}(z_2^-) = 0, \quad \phi_{2z}^{(1)}(z_2^-) &= -\frac{k}{\tanh kH_3}. \end{aligned}\right\} \tag{A 17}$$

Equation (A 16) with boundary conditions (A 17) respectively determine $\phi_{1,2}^{(1)}$ uniquely.

However, the full expressions for $\phi_{1,2}^{(1)}$ are not needed; all that is required is the $O(\epsilon)$ terms $n_{1,2}$. These are found by multiplying (A 16) by $\phi_{1,2}^{(0)}$ and integrating over U, L respectively. On using the boundary conditions (A 7), (A 17) we find that

$$\left.\begin{aligned} \frac{2\big(c^{(1)}+\Delta\big)I_1}{c_0^3} &= -\frac{\rho_1 k}{\tanh kH_1} - \rho_2 m_1^{(0)} n_1^{(1)}, \\ \frac{2\big(c^{(1)}-\Delta\big)I_2}{c_0^3} &= -\frac{\rho_3 k}{\tanh kH_3} + \rho_2 m_2^{(0)} n_2^{(1)}, \end{aligned}\right\} \tag{A 18}$$

$$\text{where} \quad I_{1,2} = \int_{U,L} \overline{\rho} N^2 \phi_{1,2}^{(0)2}\, \mathrm{d}z = \int_{U,L} \overline{\rho} c_{1,2}^2 \phi_{1z,2z}^{(0)2}\, \mathrm{d}z\,. \tag{A 19}$$

Retaining in (A 11) only the leading-order terms we find that

$$\left.\begin{aligned} D_1 &\approx \frac{2\big(c^{(1)}+\Delta\big)I_1}{\rho_2 m_1^{(0)} c_0^3} + \frac{\rho_1 k}{\rho_2 m_1^{(0)} \tanh kH_1} + \frac{m_1^{(0)} k}{\tanh kH_2}, \\ D_2 &\approx \frac{2\big(c^{(1)}-\Delta\big)I_2}{\rho_2 m_2^{(0)} c_0^3} + \frac{\rho_3 k}{\rho_2 m_2^{(0)} \tanh kH_3} + \frac{m_2^{(0)} k}{\tanh kH_2}, \\ E_1 &\approx -\frac{m_2^{(0)} k}{\sinh kH_2}, \quad E_2 \approx -\frac{m_1^{(0)} k}{\sinh kH_2}. \end{aligned}\right\} \tag{A 20}$$

Here the densities $\rho_{1,2,3}$ are the uniform values of $\overline{\rho}(z)$ in regions I, II and III, respectively. Equations (A 10) now become

$$\left.\begin{aligned} \big(c^{(1)}+\Delta\big)K_1 A + \frac{\rho_1 k}{\rho_2 m_1^{(0)} \tanh kH_1} A + \frac{m_1^{(0)} k}{\tanh kH_2} A - \frac{m_2^{(0)} k}{\sinh kH_2} B = 0, \\ \big(c^{(1)}-\Delta\big)K_2 B + \frac{\rho_3 k}{\rho_2 m_2^{(0)} \tanh kH_3} B + \frac{m_2^{(0)} k}{\tanh kH_2} B - \frac{m_1^{(0)} k}{\sinh kH_2} A = 0, \end{aligned}\right\} \tag{A 21}$$

$$\text{where} \quad K_1 = \frac{2I_1}{\rho_2 m_1^{(0)} c_0^3}, \quad K_2 = \frac{2I_2}{\rho_2 m_2^{(0)} c_0^3}\,.$$

These equations are the asymptotic outcome in Fourier space. The final step is to recall that the physical amplitudes are $(A, B)\exp(\mathrm{i}k(x-ct)$ and hence we may replace $\mathrm{i}k$ with $\partial/\partial\xi$ and $-\mathrm{i}kc^{(1)}$ with $\partial/\partial T$; here $\xi = x - c_0 t$ and T is a slow time relative to the ξ-reference frame. At this stage we also add the nonlinear terms, where it can be shown that they are just those which belong only to the uncoupled modes, and hence can be readily found from the literature (see Benjamin 1967; Davis & Acrivos 1967). Thus we obtain, now for the physical amplitudes $A(\xi, T)$, $B(\xi, T)$,

$$\left.\begin{aligned} K_1\{A_T - \Delta A_\xi\} + \gamma_U A A_\xi + \frac{\rho_1}{\rho_2 m_1^{(0)}} \mathscr{M}_1(A) + m_1^{(0)} \mathscr{M}_2(A) - m_2^{(0)} \mathscr{M}(B) = 0, \\ K_2\{B_T + \Delta B_\xi\} + \gamma_L B B_\xi + \frac{\rho_3}{\rho_2 m_2^{(0)}} \mathscr{M}_3(B) + m_2^{(0)} \mathscr{M}_2(B) - m_1^{(0)} \mathscr{M}(A) = 0, \end{aligned}\right\} \tag{A 22}$$

where, for amplitude function A

$$\mathscr{M}_j(A) = \frac{1}{2\pi} \int_{-\infty}^{\infty} \frac{-\mathrm{i}k^2}{\tanh kH_j} \widehat{A}(k, T) \mathrm{e}^{\mathrm{i}k\xi}\, \mathrm{d}k, \quad (j = 1, 2, 3), \tag{A 23}$$

$$\mathscr{M}(A) = \frac{1}{2\pi} \int_{-\infty}^{\infty} \frac{-\mathrm{i}k^2}{\sinh kH_2} \widehat{A}(k, T) \mathrm{e}^{\mathrm{i}k\xi}\, \mathrm{d}k, \tag{A 24}$$

$$\text{and} \quad \widehat{A}(k,T) = \int_{-\infty}^{\infty} A(\xi,T)\,\mathrm{e}^{-\mathrm{i}k\xi}\,\mathrm{d}\xi \tag{A 25}$$

is the Fourier transform of A. There are similar expressions for B. The nonlinear coefficients are

$$\gamma_{U,L} = \frac{3}{\rho_2 m_{1,2}^{(0)} c_0} \int_{U,L} \overline{\rho}\left(\phi_{(1,2)z}^{(0)}\right)^3 \mathrm{d}z. \tag{A 26}$$

Using the known results 861.65, 861.66 in Dwight (1961)

$$\int_{-\infty}^{\infty} \sin kx \tanh qx\,\mathrm{d}x = \frac{\pi}{q\sinh\left(\dfrac{\pi k}{2q}\right)}, \quad (q>0),$$

$$\int_{-\infty}^{\infty} \frac{\sin kx}{\tanh qx}\,\mathrm{d}x = \frac{\pi}{q\tanh\left(\dfrac{\pi k}{2q}\right)}, \quad (q>0),$$

the integrals in (A 23), (A 24) may be evaluated to yield

$$\mathscr{M}_j(A) = -\frac{1}{2H_j}\frac{\partial^2}{\partial\xi^2}\int_{-\infty}^{\infty} A(\tilde{\xi},T)\coth\frac{\pi(\xi-\tilde{\xi})}{2H_j}\,\mathrm{d}\tilde{\xi} \qquad (j=1,2,3)$$

$$\mathscr{M}(A) = -\frac{1}{2H_2}\frac{\partial^2}{\partial\xi^2}\int_{-\infty}^{\infty} A(\tilde{\xi},T)\tanh\frac{\pi(\xi-\tilde{\xi})}{2H_2}\,\mathrm{d}\tilde{\xi}.$$

Thus (A 22) become

$$\left.\begin{aligned} A_T - \Delta A_\xi + \alpha_1 A A_\xi + \beta_1 \frac{\partial^2}{\partial\xi^2}\left[\frac{\rho_1}{\rho_2}\mathscr{H}_1(A) + m_1^2\mathscr{H}_2(A) - m_1 m_2 \mathscr{H}(B)\right] = 0, \\ B_T + \Delta B_\xi + \alpha_2 B B_\xi + \beta_2 \frac{\partial^2}{\partial\xi^2}\left[\frac{\rho_3}{\rho_2}\mathscr{H}_3(B) + m_2^2\mathscr{H}_2(B) - m_1 m_2 \mathscr{H}(A)\right] = 0, \end{aligned}\right\} \tag{A 27}$$

where the operators are defined by

$$\mathscr{H}_j(A) = -\frac{1}{2H_j}\int_{-\infty}^{\infty} A(\tilde{\xi},T)\coth\frac{\pi(\xi-\tilde{\xi})}{2H_j}\,\mathrm{d}\tilde{\xi}, \quad (j=1,2,3) \tag{A 28}$$

$$\mathscr{H}(A) = -\frac{1}{2H_2}\int_{-\infty}^{\infty} A(\tilde{\xi},T)\tanh\frac{\pi(\xi-\tilde{\xi})}{2H_2}\,\mathrm{d}\tilde{\xi}, \tag{A 29}$$

while the coefficients are given by

$$\alpha_{1,2} = \frac{3}{2}\frac{\displaystyle\int_{U,L}\overline{\rho}(\phi_{1,2}')^3\,\mathrm{d}z}{\displaystyle\int_{U,L}\overline{\rho}(\phi_{1,2}')^2\,\mathrm{d}z}, \quad \beta_{1,2} = \frac{1}{2}\frac{c_{1,2}\rho_2}{\displaystyle\int_{U,L}\overline{\rho}(\phi_{1,2}')^2\,\mathrm{d}z}, \tag{A 30}$$

$$\text{and} \quad (\overline{\rho}\phi_{1,2}')' - \frac{g\overline{\rho}'}{c^2}\phi_{1,2} = 0, \quad \phi_{1,2}'(z_{1,2}^{\pm}) = 0, \tag{A 31}$$

$$\text{while} \quad \phi_1(z_1^+) = 1, \quad \phi_1(z_1^-) = m_1, \quad \phi_2(z_2^-) = -1, \quad \phi_2(z_2^+) = m_2, \tag{A 32}$$

where the zero superscript on $m_{1,2}$ and $\phi_{1,2}$ have been dropped and the prime denotes differentiation with respect to z. Equations (A 27) summarize the result of this appendix, giving the governing equations used in our paper. Note that in this

final form, the modal equations (A 31) are to be solved under the constraint that the linear long wave speeds are such that $c = c_{1,2} = c_0 \pm \Delta$ (see (A 15)).

The system of equations may be non-dimensionalized using h and $\sqrt{h/g}$ as length (L) and time (T) scales, respectively. Denoting $[Q]$ as the dimension of Q, we have $[t] = T$, $[\xi] = L$, $[c_0] = [\Delta] = L/T$, $[A] = [B] = [\mathscr{H}_j(A)] = [\mathscr{H}(A)] = L^2/T$, $[\alpha] = 1/L$, $[\beta] = L^2/T$, while both $\phi_{1,2}$ and $m_{1,2}$ are dimensionless. Replacing all variables in (24), except the density $\overline{\rho}$, by non-dimensional (say tilde) variables and subsequently dropping the tildes gives identically the same equations , except that in the modal equation gravity no longer appears explicitly, and so it becomes instead,

$$(\overline{\rho}\phi'_{1,2})' - \frac{\overline{\rho}'}{c^2}\phi_{1,2} = 0, \tag{A 33}$$

while the associated boundary conditions and normalization conditions remain the same.

To compare (A 27) with Liu *et al.* (1980) we need to allow for the different normalization of ϕ_2. That is, we must replace ϕ_2 with $m_2\tilde{\phi}_2$ and B with $\tilde{B}/m_2$ where the tilde superscript denotes the variables used by Liu *et al.* There is then complete agreement, except for an unexplained factor of two in the nonlinear coefficients (that is, the present expressions are one-half of those given in Liu *et al.* 1980); this amounts to a re-scaling of the amplitude, and does not affect the dynamics. There are also some minor differences in that the integrals we use to define the coefficients are taken over the actual pycnoclines U, L, whereas Liu *et al.* (1980) extend these integrals to infinity, a step which might introduce some errors for a density profile which is only continuous at the pycnocline boundaries.

REFERENCES

Ablowitz, M. J. & Segur, H. 1981 *Solitons and the Inverse Scattering Transform*. SIAM.

Akylas, T. R. & Grimshaw, R. H. J. 1992 Solitary internal waves with oscillatory tails. *J. Fluid Mech.* **242**, 279–298.

Benjamin, T. B. 1967 Internal waves of permanent form in fluids of great depth. *J. Fluid Mech.* **29**, 559–592.

Davis, R. E. & Acrivos, A. 1967 Solitary internal waves in deep water. *J. Fluid Mech.* **29**, 593–607.

Dwight, H. B. 1961 Table of Integrals and other Mathematical Data, 4th edn. Macmillan.

Fermi, E., Pasta, J. R. & Ulam, S. M. 1955 Studies of nonlinear problems. *Los Alamos Sci. Lab. Rep.* LA-1940.

Fornberg, B. & Driscoll, T. A. 1999 A fast spectral algorithm for nonlinear wave equations with linear dispersion. *J. Comput. Phys.* **155**, 456–467.

Gear, J. A. & Grimshaw, R. 1984 Weak and strong interactions between internal solitary waves. *Stud. Appl. Math.* **70**, 235–258.

Grimshaw, R. 2001 Internal solitary waves. In *Environmental Stratified Flows* (ed. R. Grimshaw), ch. 1, pp. 1–29. Kluwer.

Helfrich, K. R & Melville, W. K. 2006 Long nonlinear internal waves. *Annu. Rev. Fluid Mech.* **38**, 395–425.

Joseph, R. I. 1977 Solitary waves in finite depth fluid. *J. Phys.* A*: Math. Gen.* **10** (12), L225–L227.

Keulegan, G. H. 1948 Gradual damping of solitary waves. *Natl Bur. Sci. J. Res.* **40**, 487–498.

Kubota, T., Ko, D. R. S. & Dobbs, L. D. 1978 Weakly-nonlinear, long internal gravity waves in stratified fluids of finite depth. *J. Hydronaut.* **12**, 157–165.

Liu, A. K., Kubota, T. & Ko, D. R. S. 1980 Resonant transfer of energy between nonlinear waves in neighbouring pycnoclines. *Stud. Appl. Math.* **63**, 25–45.

Liu, A. K., Pereira, N. R. & Ko, D. R. S. 1982 Weakly interacting internal solitary waves in neighbouring pycnoclines. *J. Fluid Mech.* **122**, 187–194.

Malomed, B. A. 1987 "Leapfrogging" solitons in a system of coupled KdV equations. *Wave Motion* **9**, 401–411.

Ono, H. 1975 Algebraic solitary waves in stratified fluids. *J. Phys. Soc. Japan* **39**, 1082–1091.

Segur, H. 1973 The Korteweg–de Vries equation and water waves. Solutions of the equation. Part I. *J. Fluid Mech.* **59**, 721–736.

Weidman, P. D. & Johnson, M. 1982 Experiments on leapfrogging internal solitary waves. *J. Fluid Mech.* **122**, 195–213.

Weidman, P. D. & Maxworthy, T. 1978 Experiments on strong interactions between solitary waves. *J. Fluid Mech.* **85** (3), 417–431.

Wright, J. D. & Scheel, A. 2007 Solitary waves and their linear stability in weakly coupled KdV equations. *Z. Angew. Math. Phys.* **58**, 1–36.